RESEARCH ARTICLE

Key Points:
- We present a new method to kinematically image finite-fault rupture which reduces the number of basis to spatially discretize the slip
- The inversion employs a neural-network based evolutionary method that improves model estimation
- We discretize the fault using fuzzy basis functions that stabilizes the inversion and reduces the number of small singular values

Supporting Information:

Supporting Information may be found in the online version of this article.

Correspondence to:

A. Ansari,
a.ansari@iiees.ac.ir

Neuro-Fuzzy Kinematic Finite-Fault Inversion: 1. Methodology

Navid Kheirdast[1] [ID]**, Anooshiravan Ansari[1]** [ID]**, and Susana Custódio[2]** [ID]

[1]International Institute of Earthquake Engineering and Seismology (IIEES), Tehran, Iran, [2]Instituto Dom Luiz (IDL), Faculdade de Ciências, Universidade de Lisboa, Lisbon, Portugal

Abstract Kinematic finite-fault source inversions aim at resolving the spatio-temporal evolution of slip on a fault given ground motion recorded on the Earth's surface. This type of inverse problem is inherently ill posed due to two main factors. First, the number of model parameters is typically greater than the number of independent observed data. Second, small singular values are generated by the discretization of the physical rupture process and amplify the effect of noise in the inversion. As a result, one can find different slip distributions that fit the data equally well. This ill posedness can be mitigated by decreasing the number of model parameters, hence improving their relationship to the observed data. In this study, we propose a fuzzy function approximation approach to describe the spatial slip function. In particular, we use an Adaptive Network-based Fuzzy Inference System (ANFIS) to find the most adequate discretization for the spatial variation of slip on the fault. The fuzzy basis functions and their respective amplitudes are optimized through hybrid learning. We solve this earthquake source problem in the frequency domain, searching for optimal spatial slip distribution independently for each frequency. The approximated frequency-dependent spatial slip functions are then used to compute the forward relationship between slip on the fault and ground motion. The method is constrained through Tikhonov regularization, requiring a smooth spatial slip variation. We discuss how the number of model parameters can be decreased, while keeping the inversion stable and achieving an adequate resolution. The proposed inversion method is tested using the SIV1-benchmark exercise.

Plain Language Summary Earthquake kinematic source inversions help seismologists infer key features of fault ruptures from the available recorded data. The technique faces inherent ill posedness from the viewpoint of its mathematical formulation. Furthermore, the limited available datasets render the problem even more challenging. In this study, we use an adaptive function approximation methodology that describes slip on the fault using a reduced number of model parameters. This innovative formulation helps us to achieve a good balance between available data (information) and model parameters (unknowns). The proposed technique decreases the degree of ill posedness of the inverse problem by adaptively improving the slip discretization and the slip amplitude using neural network learning.

1. Introduction

Kinematic finite-fault modeling is one of the most widely used tools to image the evolution of earthquake ruptures. The finite-fault models are spatio-temporal functions that represent the evolution of slip on a fault. Such models are critical to understand the complexity of rupture mechanics (Causse et al., 2013; Gabriel et al., 2012; Heaton, 1990; Mai et al., 2016; Page et al., 2005; Thingbaijam et al., 2017; Tinti et al., 2005), including the evolution of slip on faults throughout the seismic cycle (Custódio & Archuleta, 2007; Freed & Lin, 2001) or the values and distribution of stress drop within tectonic structures (Bouchon, 1997; King et al., 1994; Mai & Beroza, 2000; Ripperger & Mai, 2004; Stein et al., 1997). Finite-fault models can also be used to develop ground-motion prediction equations (Archuleta & Ji, 2016; Atkinson & Boore, 2006; Zafarani et al., 2009) or to simulate the time history of ground shaking (Beresnev & Atkinson, 1997; Mai, 2009; Mai et al., 2010). Moreover, these models gain value in physics-based hazard assessment, which are particularly important for the hazard analysis of critical facilities, like nuclear power plants (Hutchings et al., 2007, 2018).

Finite-fault models are obtained by inverse modeling of earthquake observations (Mai et al., 2016). In order to retrieve the full spatio-temporal evolution of slip, one can use records of the dynamic wavefield, such as seismic data (Cotton & Campillo, 1995; Custódio et al., 2005; Das & Kostrov, 1990; Ji et al., 2002a, 2002b; Olson & Anderson, 1988; Olson & Apsel, 1982; Twardzik et al., 2012), high-rate GNSS/GPS data (Custódio et al., 2009; Minson et al., 2013, 2014), or tsunami data (Satake et al., 2013). Final static displacements, provided by geodetic observations, like InSAR or GNSS records, can be used to map the final cumulative displacement on the fault (Barnhart & Lohman, 2010; Lohman & Simons, 2005; Massonnet & Feigl, 1998). Records of the static and dynamic fields can be jointly used to increase the stability of inversions (e.g., Hernandez et al., 2004; Jara et al., 2018; Nissen et al., 2019).

The governing equation that relates observations on the Earth's surface with the dislocation on the fault is the representation theorem of seismology (Aki & Richards, 2002). This theorem can be used to compute ground displacement given a fault slip model, in the context of a forward problem. In the framework of an inverse problem, it can be used to find the slip model that best fits the observed data using optimization methods (Liu & Archuleta, 2004; Olson & Apsel, 1982).

The representation theorem of seismology is expressed as a Fredholm integral equation of the first kind. Therefore, inverse problems based on the representation theorem are inherently ill posed (Hansen, 2005). The ill posedness of an inverse problem reflects the instability and nonuniqueness of its solutions. The solutions of ill-posed inverse problems are very sensitive to small perturbations of the input signal, which commonly arise from noise in the data. In the realm of linear inverse problems, singular value decomposition is frequently been used to handle ill posedness (e.g., Gallovič & Ampuero, 2015). Near zero and very small singular values are responsible for the instability and nonuniqueness of the solution, and therefore require special attention (e.g., Aster et al., 2018).

An ill-posed inverse problem can be stabilized by regularization, which will approximate the ill-posed problem by a family of well-posed problems (Engl et al., 1996). In finite-fault inversion, common regularization approaches include damping small singular values, which reduces their impact; smoothing, which ensures a smooth variation of slip throughout the fault; or moment magnitude minimization, which favors slip distributions that fit the data with a minimum amount of seismic moment. These mathematically and physically motivated constraints reduce the number of preferred slip models, thus stabilizing the inversion.

In order to capture numerically the full rupture kinematics, the continuous evolution of slip on the fault must be discretized. The integral equation of the representation theorem can be approximated using either quadrature or Galerkin methods (Hansen, 2005). Kinematic finite-fault inversions typically rely on Galerkin-type discretizations, where the continuous slip distribution is expanded over basis functions both in space and in time. By discretization, the inherent difficulties of the continuous problem, which arises from the small singular values of the continuous Fredholm integral kernel, transfer directly to the discrete space. A coarse discretization transfers less small singular values than a finer discretization (Hansen, 2005).

In early methods, the continuous spatial slip distribution was simply expanded over Dirac delta basis functions. Thus, the spatial slip distribution was simply the sum of slip in subfaults with constant slip (Olson & Apsel, 1982). The slip function was therefore approximated as a summation of C^0-continuous functions, that is, the resulting slip distribution was spatially discontinuous. Later, more sophisticated approaches approximated the spatial slip distribution using higher order basis functions, thus avoiding discontinuities at the edges of sub-faults. As an example, Liu and Archuleta (2004) proposed an interpolation scheme that resulted in a C^1-continuous description of slip in space. In this case, the interpolation scheme ensured that the spatial slip distribution itself was continuous. However, the slip derivatives of order ≥1 were still discontinuous. In general, higher order basis functions help the solution estimate the data more accurately.

The discretization of the evolution of slip in time approximates the source time function for each point on the fault, that is, the history of slip at given time steps for each subfault. The temporal basis functions can also be Dirac delta functions. However, a more common approach is to use elementary functions, such as triangular functions (Hartzell & Heaton, 1983; Olson & Apsel, 1982). Beresnev (2003) addressed well the shortcomings of triangular functions to expand slip-rate functions. An alternative to assuming many base functions to discretize slip in time is to assume that the source time function at each point on the fault has a predetermined shape and is fully determined by a few key functional parameters, such as rise time and

rupture velocity (e.g., Liu & Archuleta, 2004). In this case, the number of model parameters is strongly reduced, but the shape of the source time function becomes fixed a priori. Additionally, the inversion becomes nonlinear. Hallo and Gallovič (2020) recently proposed to use a regularized Yoffe slip-rate function (Tinti et al., 2005). Their method accounts for Green's function uncertainty by using a Bayesian inversion framework with Markov Chain Monte Carlo (MCMC) sampling.

The methods described above rely on the time-domain formulation of the representation theorem. Alternatively Fan et al. (2014) used complex time-harmonic functions to approximate the time evolution of slip. Their method evaluated the representation theorem in the frequency domain. They took advantage of the fact that the time-domain convolution between source slip function and Green's functions becomes a simple multiplication in the frequency domain. In this article, we follow their approach, benefiting from the linearity of the representation theorem in the frequency domain.

As pointed out by Aster et al. (2018), the selection of appropriate basis functions for the discretization of an integral equation is rather an art. The selection of the basis functions has a direct effect on the degree of ill conditioning of the discrete inverse problem and ultimately on the quality of the solution. Such selection requires detailed knowledge of the problem and of the behavior of the basis functions. A review of a database of finite-fault solutions provided by Mai and Thingbaijam (2014) reveals that slip on faults often consists on one or two main asperities. In each asperity, the slip has its maximum value around the center of the asperity and decays bidirectionally on the fault surface. In this case, ellipses could be appropriate basis functions to describe slip on faults. Some authors have assumed that slip is localized on a few elliptical patches and solved the inverse problem to find only a few parameters that describe those elliptical patches (Di Carli et al., 2010; Twardzik et al., 2012; Vallée & Bouchon, 2004). By selecting elliptical basis functions, the dimension of the model space decreases considerably, in turn increasing the stability of the solution. In the more conventional case of constant-slip subfaults, increasing the number of sub-faults has the disadvantage of increasing the number of small singular values, hence worsening the ill posedness of the inversion and making the solution more unstable (Hansen, 2005). In general, it is possible to select a proper set of basis functions to discretize the model space in a way that reduces the number of model parameters, thus increasing the stability of the solution. In this article, we propose a new method that finds an optimal discretization of the spatial slip function using fuzzy approximation theory.

From the viewpoint of approximation theory, additive fuzzy systems can be used as uniform approximators of any continuous function to any degree of accuracy (Buckley, 1992; Kosko, 1994; Wang, 1992; Wang & Mendel, 1992). Adaptive fuzzy systems approximate continuous functions globally by using overlapping patches and locally by tuning the fuzzy patches using a neural system (Kosko, 1994). Among existing fuzzy systems, Jang (1991) implemented the Takagi-Sugeno fuzzy system (Takagi & Sugeno, 1983) in the context of neural networks, which resulted in the Adaptive Network-based Fuzzy Inference System (ANFIS). Here, we use ANFIS to approximate the spatial component of the earthquake source function.

In linear approximation theory, a general function can be approximated by a summation of unknown scalar parameters multiplied by known basis functions. For example, in Fourier series approximation, any periodic function can be approximated by a summation of unknown scalar coefficients multiplied by known sinusoids. ANFIS is a type of nonlinear function approximator where only the functional form of the basis functions are known a priori. The final form of the basis functions, in addition to the approximation coefficients, are obtained in a process of learning. Learning in adaptive network theory is simply solving an optimization problem to find the unknowns.

In this article, we use the approximation power of ANFIS to discretize the spatial component of the representation theorem of seismology. Using this new discretization scheme, we propose a new inversion methodology that describes slip on the fault in terms of only a few C^∞-continuous basis functions which are found by fuzzy approximation. The inversion is carried out in the frequency domain, such that a spatial slip distribution is found independently for each frequency. For each frequency, the spatial slip distribution is obtained through a hybrid inversion scheme, which iteratively solves for the basis functions (nonlinear inversion) and their amplitudes (linear inversion). The parameters of the basis functions are found using gradient descent, whereas their amplitudes are found through linear least squares inversion (Jang, 1993). The

inversion is regularized using spatial smoothing by Tikhonov regularization. The optimal degree of spatial smoothing is resolved by smoothness versus misfit L-curves (Hansen, 2005), which display sharp corners.

The performance of the method is assessed using the SIV1 benchmark exercise (http://equake-rc.info/sivdb/wiki/Downloads) (Mai et al., 2016). This benchmark has been solved before using a wide range of finite-fault inversion algorithms. In order to rank the success of different finite-fault algorithms and their solutions, Razafindrakoto et al. (2015) developed the multidimensional scaling method. The multidimensional scaling analysis of SIV1 solutions showed that the results of Fan et al. (2014) and Gallovič and Zahradník (2011) obtained the best results. Fan et al. (2014) used a frequency-domain formulation and solved the inversion using a Bayesian approach. Regularization constraints included penalizing nonsmooth spatial slip distributions, damping small singular values, and fixing slip at fault boundaries. Gallovič and Zahradník (2011) used a time domain formulation with a large space-time model space, which later upgraded (Gallovič et al., 2015). Their regularization constraints included a target seismic moment and truncation of low singular values. We present our solution of the SIV1 benchmark exercise, using different number of fuzzy basis functions and discuss their effect on regularization.

In a companion article (Kheirdast et al., 2020), we apply the neuro-fuzzy method presented here to real data, in particular to the well-studied Mw 6.2, 24/August/2016, Amatrice earthquake. Therein, we invert two different ground motion data sets, including GNSS ground displacements and strong-motion records. The low-frequency components of slip ($f <= 0.06$ Hz) are inferred from static and high-rate GNSS data, whereas higher frequencies ($f > 0.06$ Hz) are inferred from accelerograms. The companion article discusses the many challenges of modeling real data, including how to set a proper regularization parameter and how to select an appropriate spatial discretization. The accuracy of the inferred kinematic model in the frequency range of the accelerograms ($0.06 < f < 0.5$ Hz) is assessed by comparing synthetics with high-rate GNSS data excluded from the inversion dataset. The good match between synthetic waveforms inferred from the kinematic model and the observed, noninverted, high-rate GNSS displacements confirms the reliability of the method.

2. Method

In this section, we present a new method to compute kinematic finite-fault models based on an Adaptive Neuro-Fuzzy Inference System (ANFIS). We start by presenting the forward relationship, which consists of the representation theorem of seismology (Section 2.1). The frequency-domain formulation of the representation theorem allows us to solve independently for the spatial slip distribution at each frequency. Thus, the time domain 3D spatio-temporal inverse problem is reduced to several smaller independent 2D inversions in the frequency domain. We then introduce the adaptive fuzzy approximation that is used to find both the optimal basis functions and their amplitudes, which together describe the spatial distribution of slip at each frequency (Section 2.2). This optimized spatial discretization allows to lower the number of model parameters. In Section 2.2.1, we introduce the mathematical principles of fuzzy approximation and show how parameters (i.e., the basis functions and their amplitudes) can be found using an ANFIS. Section 2.2.2 shows how the fuzzy source description can be combined with Green's functions in order to obtain synthetic waveforms. Finally, Section 2.2.3 shows how an appropriate finite-fault kinematic model can be found by optimizing data fit and simultaneously applying a smoothness regularization constraint. Text S1 describes in detail how ANFIS is used to describe the 2D spatial slip distributions. Text S2 describes how to train the model parameters of the ANFIS, that is, how to optimize the basis functions of the spatial slip distribution and their amplitudes. Text S3 explains the Gaussian integration method that we use to generate synthetic ground motion from the integration of slip on the fault plane.

2.1. Representation Theorem: From Fault Slip to Ground Motion

The representation theorem of seismology describes the surface displacement, $\mathbf{u}^o$, that is generated by an earthquake source $\mathbf{u}^f$, assuming that the response of the Earth is that of a linear elastic solid (Aki & Richards, 2002). The representation theorem can be written in the time domain using a convolutional integral, which integrates slip throughout the fault and convolves it with Green's functions:

$$u_n^o(\mathbf{x},t) = \int_{-\infty}^{+\infty} d\tau \int_\Gamma u_i^f(\boldsymbol{\xi},\tau) c_{ijpq} v_j \frac{\partial}{\partial(\xi_q)} G_{np}(\mathbf{x}, t-\tau; \boldsymbol{\xi}, 0) d\Gamma \tag{1}$$

where, $u_n^o(\mathbf{x},t)$, $n = 1,2,3$, is the n'th component of the displacement vector on the Earth surface at location $\mathbf{x}$ and time t. The seismic source displacement is described as slip, $u_i^f(\boldsymbol{\xi},\tau)$, occurring in point $\boldsymbol{\xi}$ and time τ over a fault plane Γ. c_{ijpq} is the elasticity tensor and v_j is the j'th component of the vector normal to the fault plane. $G_{np}(\mathbf{x}, t-\tau; \boldsymbol{\xi}, 0)$ is the Green's function that represents the displacement at point $\mathbf{x}$ and time $t-\tau$ on the Earth surface due to a point force applied at time 0 and location $\boldsymbol{\xi}$ within the solid Earth.

The time-domain convolution of slip on the fault with Green's functions becomes a simple multiplication in the frequency domain:

$$u_n^o(\mathbf{x},\omega) = \int_\Gamma u_i^f(\boldsymbol{\xi},\omega) c_{ijpq} v_j \frac{\partial}{\partial(\xi_q)} G_{np}(\mathbf{x},\omega; \boldsymbol{\xi}) d\Gamma \tag{2}$$

Note that the source function can be described in space and time, $u_i^f(\boldsymbol{\xi},\tau)$, or equivalently in space and frequency, $u_i^f(\boldsymbol{\xi},\omega)$, where ω denotes the angular frequency. In the present application, the source function is inferred from seismic data, which can also be provided as waveforms in the time domain, $u_n^o(\mathbf{x},t)$, or as spectra in the frequency domain, $u_n^o(\mathbf{x},\omega)$. Identically, the Green's functions, which contain the response of the Earth to applied seismic moments, can be computed in time, $G_{np,q}(\mathbf{x}, t-\tau; \boldsymbol{\xi}, 0)$, or in frequency, $G_{np,q}(\mathbf{x},\omega; \boldsymbol{\xi})$. In Equations 1 and 2, displacements can be replaced by velocities without loss of generality by using the adequate replacements. For example, the source velocity function (SVF), or slip-rate (Figure S4), which we aim to find, is simply given by $\dot{u}_i^f(\boldsymbol{\xi},\tau)$ in the time domain or equivalently by $i\omega u_i^f(\boldsymbol{\xi},\omega)$ in the frequency domain.

Let us consider that the fault is approximately a planar surface. Then, the source function becomes a function of three independent variables, $u_i^f(\xi,\eta,\tau)$, or $u_i^f(\xi,\eta,\omega)$, where ξ is the spatial coordinate along the strike of the fault and η is the spatial coordinate up the dip of the fault, that is, $\boldsymbol{\xi} = (\xi,\eta) \in \Gamma$. Using the frequency-domain formulation of the representation theorem (Equation 2), the problem can be solved independently for each frequency point ω_j (Figure S5). At each frequency, ω_j, the problem reduces to finding a vector function of two spatial variables $u_i^f(\xi,\eta,\omega_j)$, that fits the observed spectra, at that frequency, at the various recording stations and spatial directions. Whereas the convolutional integral of the representation theorem in the time-domain (Equation 1) results in one large 3-dimensional inverse problem, in the frequency-domain (Equation 2) we instead solve several smaller 2-dimensional inverse problems.

2.2. The Neuro-Fuzzy Inversion Method

2.2.1. Principles of Fuzzy Function Approximation

Approximation theory studies the process of approximating a general function by means of basis functions, such as polynomials, exponentials or trignometrics. Fourier series, Taylor expansion or the Finite Element method are all examples of approximating general functions using basis functions (Cohen, 2003). In general, the approximation of a general function $f(\xi)$ can be written as:

$$f(\xi) \approx \tilde{f}(\xi) = \Sigma_{i=1}^n A_i \phi_i(\xi) \tag{3}$$

where $\tilde{f}(\xi)$ is the approximated function, $\phi_i(\xi)$ are the basis functions and A_i are the approximation coefficients. The approximation error is given by the cost function:

$$Cost = \left\| f - \tilde{f} \right\|_p \tag{4}$$

In Equation 4, $\left\| \cdot \right\|_p$ represents the p'th norm, typically $p = 2$, corresponding to the Euclidean (L2) norm. If the basis functions, $\phi_i(\xi)$, are independent from the function to approximate, $f(\xi)$, then the approximation is linear. Fourier series decomposition is an example of a linear approximation. No matter the function to approximate, the basis functions are always the same sinusoids. In nonlinear, or adaptive approximation, the basis functions depend on the function to approximate. Nonlinear approximations are superior
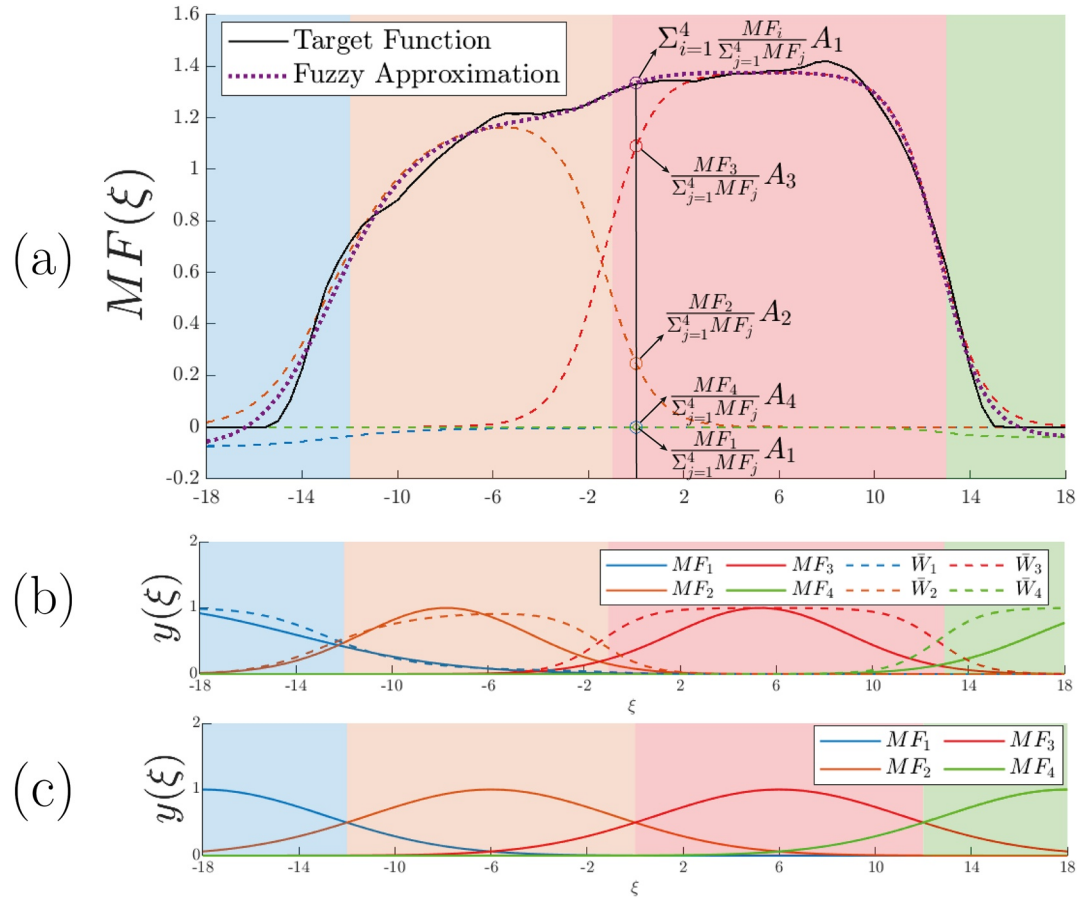
Figure 1. Example of a fuzzy function approximation. (a) The black line shows a general function that we wish to approximate. The fuzzy approximation (dotted line) is composed by scaled fuzzy basis functions (dashed lines). (b) Each fuzzy basis function (ϕ_i, dashed lines) is built from Gaussian membership functions (*MFs*) (solid lines), which cover the domain of the independent variable, ξ. (c) MFs at the first step of the learning procedure.

because the basis functions adapt to the function to approximate, thereby improving the approximation. Fuzzy function approximation is a special case of adaptive approximation. Other adaptive methods have been used successfully in Geophysics, namely the Reversible-jump method (Bodin & Sambridge, 2009; Green, 1995; Sen & Biswas, 2017), which has been introduced in seismic tomography.

Figure 1 schematically depicts the idea of fuzzy function approximation. Figure 1a shows a general target function that we wish to approximate (solid black line). The approximated function (dotted purple line) is obtained by adding scaled basis functions, $A_i\phi_i(\xi)$ (dashed colored lines). In this case, the basis functions ($\phi_i(\xi)$) are partially overlapping fuzzy clusters (dashed lines in Figure 1b). The basis functions (fuzzy clusters) are themselves composed from fuzzy patches, named membership functions (*MFs*), which cover the input domain (full lines in Figure 1b), such that:

$$f(\xi) \approx \tilde{f}(\xi) = \Sigma_{i=1}^n \frac{MF_i(\xi)}{\Sigma_{j=1}^n MF_j(\xi)} A_i \qquad (5)$$

*MF*s have values between zero and one, which represent the partial degree of belonging of a given input point (ξ) to a membership function. Thus, a point of the input domain may belong to all basis functions with different degrees of membership. In the example presented here, the four initial membership functions are regularly spaced (Figure 1c), but they evolve, or adapt, to best approximate the target function (Figure 1b). The target function $f(\xi)$ is finally approximated as a weighted summation of basis functions (Figure 1a).

The implementation of fuzzy function approximation uses fuzzy inference systems (FIS), which find the optimal membership functions, which in turn form clusters (basis functions) (Figure 1b) based on principles of fuzzy logic. In our work, we use the constant-output Takagi-Sugeno FIS (Takagi & Sugeno, 1983), where $\phi_i(\xi) = \overline{W}_i = \frac{MF_i}{\Sigma_{j=1}^n MF_j}$ are the approximation basis functions and A_i are the approximation coefficients. Systems that rely on this fuzzy function approximation are named additive fuzzy systems (Buckley, 1992; Kosko, 1994; Wang, 1992). Wang and Mendel (1992) proved that additive fuzzy systems are uniform approximators of any real continuous function to any degree of accuracy.

It is possible to expand Equation 5 using various types of membership functions (e.g., triangular, trapezoidal, Bell function, etc). In our work, we used Gaussian membership functions, $MF = gmf$, to approximate slip because they are smooth (infinitely derivable) and their shapes are fully determined by only two parameters, standard deviation, σ, and center value, μ:

$$gmf_i(\xi, \sigma_i, \mu_i) = \exp\left(\frac{-(\xi - \mu_i)^2}{2\sigma_i^2}\right) \tag{6}$$

The formulation described above can be extended to functions of any number of independent input variables. For a two-variable function, Equation 5 becomes:

$$f(\xi, \eta) \approx \tilde{f}(\xi, \eta) = \Sigma_{i=1}^n \frac{MF_i(\xi, \eta)}{\Sigma_{j=1}^n MF_j(\xi, \eta)} A_i \tag{7}$$

where the membership functions are now two-dimensional functions, $MF(\xi, \eta)$, which can be obtained from the one-dimensional ones by simple multiplication: $MF(\xi, \eta) = MF(\xi) \times MF(\eta)$.

The approximation problem now consists of finding the membership functions, MF_i, that compose the basis functions, and the respective approximation coefficients, A_i, such that the approximation error, $Cost$, is minimized. In general, this will be a nonlinear optimization problem. Jang (1991) introduced Adaptive Neuro Fuzzy Inference Systems (ANFIS) by blending the concepts of FIS and neural networks to solve this optimization problem. Several global optimization techniques have been used to solve this problem, such as genetic algorithms (GA-ANFIS) or particle swarm methods (PSO-ANFIS) (e.g., Rezakazemi et al., 2017). Jang (1993) proposed the hybrid learning method, which iteratively uses gradient descent to find the nonlinear parameters and least squares to find the linear parameters of the approximation. Text S1 describes in detail how ANFIS is used in our inversion to approximate the 2D spatial slip distribution at each frequency.

2.2.2. Representation Theorem Expanded Over a FIS Basis

Slip on a fault plane can be mapped to ground motion using the representation theorem. Considering that the slip vector can be decomposed into along-strike, $u_s(\xi, \eta, \omega)$, and updip, $u_d(\xi, \eta, \omega)$, components, slip on the fault plane can then be represented as:

$$\mathbf{u}^f(\xi, \eta, \omega) = \begin{bmatrix} \mathbf{v}_s & \mathbf{v}_d \end{bmatrix} \begin{bmatrix} u_s(\xi, \eta, \omega) \\ u_d(\xi, \eta, \omega) \end{bmatrix} \tag{8}$$

where $\mathbf{v}_s$ and $\mathbf{v}_d$ are the unit vectors along-strike and updip on the fault surface, respectively. For the sake of simplicity, we will only consider here the strike-slip component of slip: $\mathbf{u}^f(\xi, \eta, \omega) = \mathbf{v}_s u_s(\xi, \eta, \omega)$. In the remaining of the manuscript, we omit the subscript $_s$ from $u_s(\xi, \eta, \omega)$ for easiness of reading. The generalization of this formulation to both along-strike and updip components is straightforward and one such example can be found in the companion article (Kheirdast et al., 2020).

For each frequency, ω_j, we can approximate the continuous 2D spatial slip distribution using a fuzzy formulation (FIS):

$$u(\xi, \eta, \omega_j) = \sum_{i\xi=1}^{N_\xi} \sum_{i\eta=1}^{N_\eta} \overline{W}_{i\xi, i\eta, \omega_j}(\xi, \eta) A_{i\xi, i\eta, \omega_j} \qquad (\xi, \eta) \in \Gamma \tag{9}$$

where $\bar{W}_{i\xi,i\eta,\omega_j}(\xi,\eta)$ are the adaptive basis functions, composed from 2D Gaussian membership functions, and $A_{i\xi,i\eta,\omega_j}$ are the approximation coefficients, both to be found from data. Note that the amplitudes, $A_{i\xi,i\eta,\omega_j}$, are complex-value variables. Because in general, $A_{i\xi,i\eta,\omega_j}$ are complex numbers, the fuzzy system represents both the phase and amplitude information of the ground motion (Equation 9). Considering the representation theorem (Equation 2), we can then write the observed displacement at the surface as:

$$u_n^o(\mathbf{x},\omega_j) = \sum_{i\xi=1}^{N_\xi} \sum_{i\eta=1}^{N_\eta} \int_\Gamma \bar{W}_{i\xi,i\eta,\omega_j}(\xi,\eta) G_n^{'}(\mathbf{x};\xi,\eta,\omega_j) A_{i\xi,i\eta,\omega_j} d\Gamma \qquad (\xi,\eta) \in \Gamma \tag{10}$$

where Γ is the fault plane and:

$$G_n^{'} = v_{si} c_{ijpq} v_j \frac{\partial}{\partial_{\xi_q}} G_{np} \tag{11}$$

Equation 10 describes ground motion as a function of slip on the fault, which in turn is described as a combination of a few adaptive basis functions, $\bar{W}_{i\xi,i\eta,\omega_j}(\xi,\eta)$ and their amplitudes, $A_{i\xi,i\eta,\omega_j}$. In Equation 11, v_{si} denotes the i'th component of the along-strike unit vector $\mathbf{v}_s$.

We use the efficient Gauss quadrature method to compute the spatial integral of slip on the fault (Equation 10). The method is described in detail in Text S3. We start by dividing the fault plane Γ into square subfaults Γ_i (Figure 2a). We then replace the physical coordinates along-strike and updip (ξ,η) by natural integration coordinates (ϵ,δ) (Figure 2f), which facilitate Gaussian quadrature. The forward equation (Equation 10) on each integration element Γ_i then becomes (Equation 12):

$$\int_{\Gamma_i} \bar{W}_{i\xi,i\eta,\omega_j}(\xi,\eta) G_n^{'}(\mathbf{x};\xi,\eta,\omega_j) A_{i\xi,i\eta,\omega_j} d\Gamma =$$
$$\int_{\epsilon=-1}^{+1} \int_{\delta=-1}^{+1} \bar{W}_{i\xi,i\eta,\omega_j}(\xi(\epsilon,\delta),\eta(\epsilon,\delta)) G_n^{'}(\mathbf{x};\xi(\epsilon,\delta),\eta(\epsilon,\delta),\omega_j)$$
$$A_{i\xi,i\eta,\omega_j} J(\xi,\eta;\epsilon,\delta) d\epsilon \, d\delta \tag{12}$$
$$\approx \sum_{ig=1}^{M} \sum_{jg=1}^{N} \bar{W}_{i\xi,i\eta,\omega_j}(\xi(\epsilon_{ig},\delta_{ig}),\eta(\epsilon_{jg},\delta_{jg})) G_n^{'}(\mathbf{x};\xi(\epsilon_{ig},\delta_{ig}),\eta(\epsilon_{jg},\delta_{jg}),\omega_j)$$
$$\times w_{ig} w_{jg} J(\xi,\eta;\epsilon_{ig},\delta_{ig}) A_{i\xi,i\eta,\omega_j}$$

By definition, the total area of each integration element in natural coordinates equals 4, a consequence of how integration elements are defined. Therefore, if the area of integration elements in physical coordinates is S, then the natural to physical coordinates transformation kernel $J(\xi,\eta;\epsilon_i,\delta_j)$ equals $S/4$.

Note that in order to evaluate Equation 10, we must calculate the Green's functions at every Gaussian integration point. Let us consider the same number of Gaussian points along-strike and updip for each integration element, such that $M = N = N_g$. Then, Equation 10 at an observation point $\mathbf{x}_{is}$ gives:

$$u_n^o(\mathbf{x}_{is},\omega_j) = \sum_{i\xi=1}^{N_\xi} \sum_{i\eta=1}^{N_\eta} \sum_{\Gamma_i} \sum_{ig=1}^{N_g} \sum_{jg=1}^{N_g} \bar{W}_{i\xi,i\eta,\omega_j}(\xi(\epsilon_{ig,\Gamma_i},\delta_{ig,\Gamma_i}),\eta(\epsilon_{jg,\Gamma_i},\delta_{jg,\Gamma_i}))$$
$$G_n^{'}(\mathbf{x}_{is};\xi(\epsilon_{ig,\Gamma_i},\delta_{ig,\Gamma_i}),\eta(\epsilon_{jg,\Gamma_i},\delta_{jg,\Gamma_i}),\omega_j) w_{ig} w_{jg} \frac{S}{4} A_{i\xi,i\eta,\omega_j} \tag{13}$$

where ϵ_{ig,Γ_i} is the ig-th Gaussian point along-strike and δ_{jg,Γ_i} is the jg-th Gaussian point updip, in both cases within subfault Γ_i.

Equation 13 is now a set of linear equations in which $u_n^o(\mathbf{x}_{is},\omega_j)$ is the synthetic data vector containing observations at frequency ω_j and station $\mathbf{x}_{is}$. The number of elements within the synthetic data vector $u_n^o(\mathbf{x}_{is},\omega_j)$ is $N_s \times 3$, where N_s is the number of stations. On the right-hand side, $A_{i\xi,i\eta,\omega_j}$ are the amplitudes of the 2D adaptive basis functions, $\bar{W}_{i\xi,i\eta,\omega_j}$. We can simplify the equation above by re-arranging it into matrix form. To this end, we order sequentially the 2D slip amplitudes, $A_{i\xi,i\eta,\omega_j}$, in A_{ibasis} and the observations at each station and ground motion component, $u_n^o(\mathbf{x}_{is},\omega_j)$, in d_{irec}. We use the following indexing scheme:

$$ibasis = (i\xi - 1) \times N_\eta + i\eta$$

$$irec = (is - 1) \times 3 + n$$
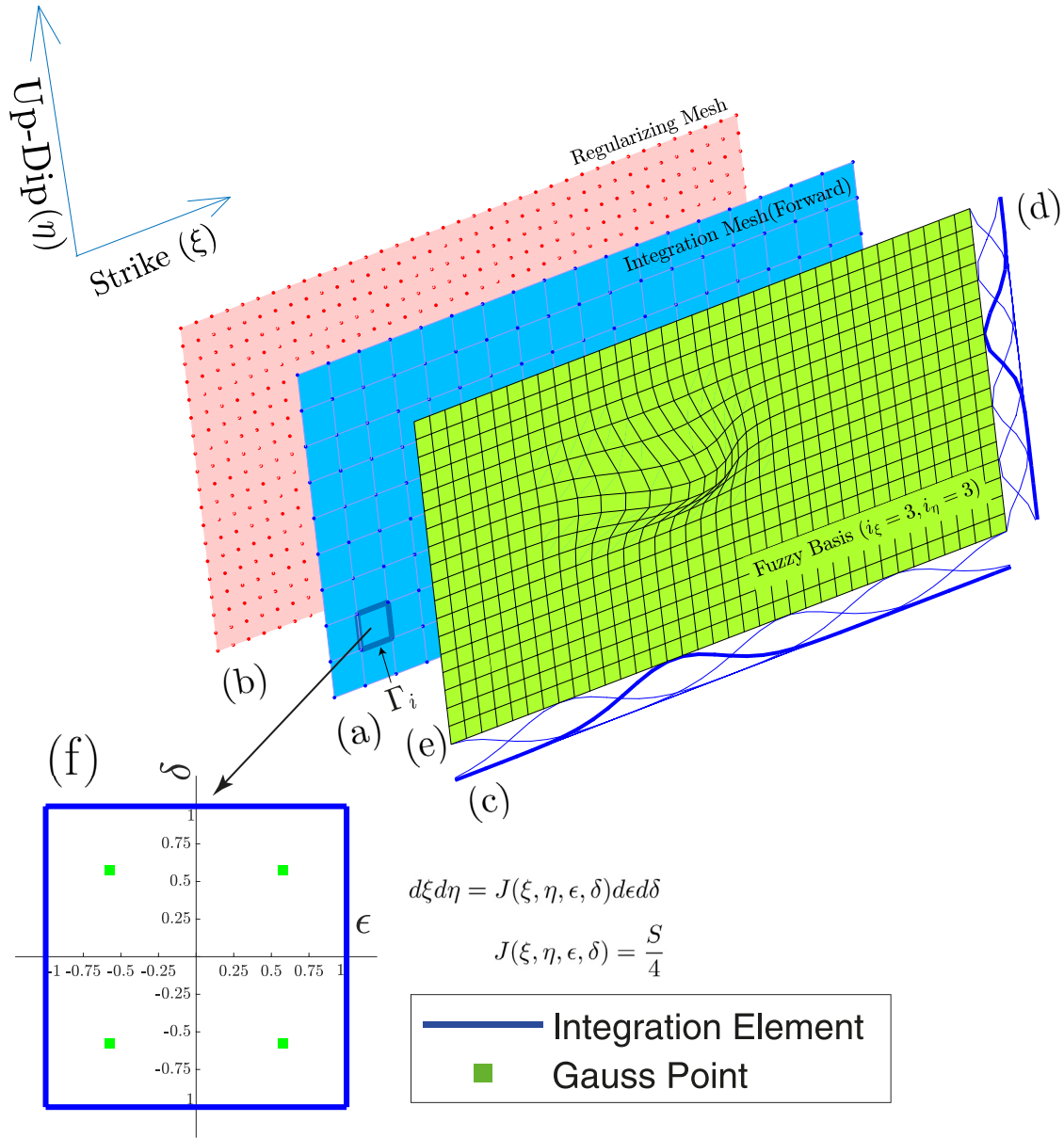
Figure 2. (a) Integration subfaults (blue points), each of which contains four Gaussian integration points (blue square in (f)), where the Green's functions are computed and used to integrate slip over the fault plane. (b) Set of regularization points, spaced 1 km × 1 km apart, used to evaluate Equation 18. (c, d) Initial 1D Gaussian fuzzy membership functions for the input variable ξ (c) and η (d). This example shows the fault discretized using 6 membership functions both along-strike and dip. (e) Initial 2D base function $\bar{W}_{i\xi=3,i\eta=3}$, which results from the combination of the third membership function along strike with the third membership function in the dip direction. This is one of the $6 \times 6 = 36$ initial basis functions used to discretize the spatial slip distribution for each frequency. (f) Integration element with four Gaussian points.

In which, each set $(i\xi, i\eta)$ corresponds to a unique $(ibasis)$ and each set (is, n) corresponds to a unique observation record $(irec)$. The forward equation that relates the amplitude vector (A_{ibasis}) with the station-component record of ground motion (d_{irec}) at frequency ω_j is mediated both by the Green's functions and by the adaptive fuzzy basis functions, which we represent as $(GW_{\omega_j})_{irec,ibasis}$:

$$(GW_{\omega_j})_{irec,ibasis} = \sum_{\Gamma_i} \sum_{ig=1}^{N_g} \sum_{jg=1}^{N_g} \bar{W}_{i\xi,i\eta,\omega_j}(\xi(\epsilon_{ig,\Gamma_i}, \delta_{jg,\Gamma_i}), \eta(\epsilon_{ig,\Gamma_i}, \delta_{jg,\Gamma_i}))$$

$$G'_n(\mathbf{x}_{is}; \xi(\epsilon_{ig,\Gamma_i}, \delta_{jg,\Gamma_i}), \eta(\epsilon_{ig,\Gamma_i}, \delta_{jg,\Gamma_i}), \omega_j) w_{ig} w_{jg} \frac{S}{4}$$

(14)

The 2D inverse problem that we need to solve for each frequency, ω_j, is then:

$$\mathbf{d}_{\omega_j} = \mathbf{GW}_{\omega_j}\mathbf{A}_{\omega_j} \tag{15}$$

This equation describes the relationship between data and the parameters of the ANFIS. Data, $\mathbf{d}$, is a known. We need to find both the basis functions, $\overline{W}_{ibasis,\omega_j}$, from which we can compute the forward relationship, $\mathbf{GW}_{\omega_j}$, and we also need to find their amplitudes, $\mathbf{A}_{\omega_j}$.

Equation 15 allows to optimize the unknown parameters, $\overline{W}_{ibasis,\omega_j}$ and $\mathbf{A}_{\omega_j}$, by fitting synthetics to data. This optimization problem is solved using the hybrid scheme described in the next section. Once the ANFIS is trained, the optimal approximation parameters have been found. The combined approximation parameters yield the kinematic slip distribution.

2.2.3. Inversion and Regularization

The optimal ANFIS approximation parameters can be found by hybrid learning (Jang, 1993). This optimization method iterates between a linear least squares inversion to find $\mathbf{A}_{\omega_j}$ and a gradient descent to find the nonlinear parameters of the basis functions, $\overline{W}_{i\xi,i\eta,\omega_j}$. At the linear step of the hybrid scheme, $\mathbf{A}_{\omega_j}$ is obtained from the inversion of Equation 15 by minimizing the L2-norm difference between data ($\mathbf{d}_{\omega_j}$) and the forward prediction ($\mathbf{GW}_{\omega_j}\mathbf{A}_{\omega_j}$):

$$\left\| \mathbf{GW}_{\omega_j}\mathbf{A}_{\omega_j} - \mathbf{d}_{\omega_j} \right\|_2 \tag{16}$$

The optimal set of amplitudes ($\mathbf{A}_{\omega_j}$) can then be found simply as:

$$\mathbf{A}_{\omega_j} = (\mathbf{GW}_{\omega_j}^T\mathbf{GW}_{\omega_j})^{-1}\mathbf{GW}_{\omega_j}^T\mathbf{d}_{\omega_j} \tag{17}$$

Because of ill posedness, the solution to Equation 17 can become unstable, that is, low noise levels may change substantially the amplitudes $\mathbf{A}_{\omega_j}$. In order to stabilize the inversion, we apply a smoothness constraint. This regularization aims to find the slip distribution with the least complexity that can fit the data well.

For sake of stability, it is advantageous to use a set of regularization points that is generally noncollocated with the set of integration points (later discussed in Section 5.5). Equation 9 can be evaluated over a set of N_{reg} regularization points, (ξ_{ireg},η_{ireg}), by applying $ibase = (i\xi - 1) \times N_\eta + i\eta$

$$u_{\omega_j}(\xi_{ireg},\eta_{ireg}) = \sum_{i\xi=1,i\eta=1}^{N_\xi \times N_\eta} \overline{W}_{i\xi,i\eta,\omega_j}(\xi_{ireg},\eta_{ireg})A_{ibase,\omega_j}, \tag{18}$$

which can be written in matrix form as:

$$\mathbf{u}_{\omega_j} = \mathbf{W}_{reg,\omega_j}\mathbf{A}_{\omega_j} \tag{19}$$

We aim to find a regularized solution consisting of the smoothest (least complex) slip distribution that can fit the data well. Thus, we require that two optimization conditions be satisfied: (a) a good fit between data and synthetics, with an allowed error δ and (b) minimization of the slip Laplacian:

$$\min \quad \begin{array}{c} \left\| \mathbf{GW}_{\omega_j}\mathbf{A}_{\omega_j} - \mathbf{d}_{\omega_j} \right\|_2 < \delta \\ \left\| \mathbf{LW}_{reg,\omega_j}\mathbf{A}_{\omega_j} \right\|_2 \end{array} \tag{20}$$

where $\mathbf{L}$ is the matrix representation of Laplacian operator (∇^2), here computed over the two-dimensional fault plane. $\mathbf{L}$ works as a roughening matrix, giving preference to smoother slip distributions. The solution that simultaneously satisfies the two optimization conditions of Equation 20 can be found by Tikhonov regularization, where the regularization parameter α is introduced (Equation 21):

$$\min \left\| \begin{bmatrix} \mathbf{GW}_{\omega_j} \\ \alpha\mathbf{LW}_{reg,\omega_j} \end{bmatrix} \mathbf{A}_{\omega_j} - \begin{bmatrix} \mathbf{d}_{\omega_j} \\ 0 \end{bmatrix} \right\|_2^2 \tag{21}$$

The solution to Equation 21 can be found by least squares inversion (Equation 22):

$$(\mathbf{GW}_{\omega_j}^T \mathbf{GW}_{\omega_j} + \alpha^2 (\mathbf{LW}_{reg,\omega_j})^T \mathbf{LW}_{reg,\omega_j})\mathbf{A}_{\omega_j} = \mathbf{GW}_{\omega_j}^T \mathbf{d}_{\omega_j} \tag{22}$$

The regularization parameter α can be physically interpreted as a smoothness-controlling parameter. The optimal smoothness level is found by L-curve diagrams (Hansen, 2005), which measure the trade-off between model smoothness and data fit. The optimal trade-off is the point where the L-curve shows a maximum curvature. This point corresponds to the smoothest model that can fit the data well. Note that in situations where the amplitude of data noise is known, the discrepancy principle can be applied to compute directly α (Aster et al., 2018). Other mathematical principles such as the discrete Picard condition (Hansen, 2005) can also be used to determine α. Note also that the optimal level of smoothness is frequency-dependent.

The cost function to be minimized by the hybrid inversion scheme is then:

$$Cost_{FIM} = \underbrace{\left\| \mathbf{GW}_{\omega_j} \mathbf{A}_{\omega_j} - \mathbf{d}_{\omega_j} \right\|_2^2}_{Cost\,data} + \alpha^2 \underbrace{\left\| \mathbf{LW}_{reg,\omega_j} \mathbf{A}_{\omega_j} \right\|_2^2}_{Cost\,smooth} \tag{23}$$

$Cost_{FIM}$ in Equation 23 is the cost function to be minimized in the neuro-fuzzy inversion. The hybrid optimization iterates between two steps. At step one, the linear parameters, $\mathbf{A}_{\omega_j}$, are found from equation Equation 22. At step two, the linear parameters are kept constant and the derivatives of $Cost_{FIM}$ (Equation 23) with respect to the nonlinear parameters, $\overline{W}_{i\xi,i\eta,\omega_j}$ (Equations 14 and 18), are computed. The nonlinear parameters are then corrected considering the derivatives using the method of gradient descent. These two steps of hybrid learning are applied iteratively until $Cost_{FIM}$ arrives at a stationary point. Text S2 explains in the detail the optimization procedure implemented by hybrid learning.

3. Synthetic Test

3.1. The SIV-inv1 Benchmark Exercise

The Source Inversion Validation (SIV) project (http://equake-rc.info/SIV/) provides several benchmark exercises to test the performance of finite-fault kinematic inversion algorithms (Mai et al., 2016). The exercises consist of slip distributions and their resulting synthetic ground motion. Users are invited to invert the synthetic ground motion using their codes. The quality of the resulting slip distributions can then be assessed by comparison with the original ones. We test the performance of our method using synthetic data from the benchmark exercise one of SIV (SIV-inv1).

SIV-inv1 corresponds to a strike-slip earthquake on a 80° dipping fault. The slip distribution was obtained from a crack-like spontaneous dynamic rupture model and is thus physically self-consistent. The fault plane is 36-km long and 18-km wide. The seismic moment of the earthquake is $M_0 = 1.06 \times 10^{19}$ N · m, corresponding to a $M_w = 6.6$ earthquake. Noise-free synthetic seismograms are available at 40 near-fault stations (Figure S6a). The sampling rate of the synthetic records is 25 Hz and the maximum frequency content of the records is $f_{max} \sim 2.5$ Hz.

The origin of the coordinate system is placed in the middle of the fault trace, at the surface. The hypocenter is located at 9.10 km E, –1.5802 km N, and at a depth of 13.9618 km. The material properties are considered to be known and made available to modelers. The velocity structure is 1D and depth dependent (Figure S6b). Velocity layers are homogeneous and isotropic. Attenuation is zero everywhere in the medium ($Q_p = Q_s = \infty$).

3.2. Inversion Setup

We computed Green's functions using AXITRA (Coutant, 1989). AXITRA implements a discrete wave-number method to forward compute seismograms corresponding to wave propagation through a layered structure (Coutant, 1989). Considering the distance between stations and fault plane, we computed Green's functions with a duration $T = 32$ s and a sampling frequency of 4 sps. The max-

imum frequency that is well represented in our Green's functions is then the Nyquist frequency $f_{Nyq} = f_{samp} / 2 = 2$ Hz. We therefore have $n2 = 128 / 2 = 64$ unique spectral points, ranging from 0 to $f_{Nyq} = 2$ Hz, with a spectral sampling of $\Delta f = f_{Nyq} / n2 = 1 / 32$ Hz. Note that both the real and imaginary parts of the spectra must be fit in order to retain the amplitude and phase information of the seismic wavefield.

We adopted the SIV-inv1 coordinate system. Accordingly, the fault plane ranges -18 km $< \xi < +18$ km along strike and 2.014 km $< \eta < 20.014$ km down dip. As explained in Section 2.2.2, we integrated slip on the fault using Gaussian integration. Each integration subfault has dimensions of 2 km × 2 km, each of which containing four Gaussian integration points (Figure 2f). We computed Green's functions for every Gaussian integration point (Figures 2a and 2f). These are the quadrature points used to evaluate Equation 14. The points used for regularization are defined on the same fault plane but distributed over a regular mesh of 1 km × 1 km, which is used to evaluate Equation 18 (Figure 2b).

As explained in Section 2.2.2, for each frequency, the spatial slip distribution is expanded using 2D adaptive fuzzy basis functions. These 2D fuzzy basis functions are obtained from the combination of 1D Gaussian membership functions distributed along-strike and updip. Here, we present results using six fuzzy membership functions for each direction, $N_\xi = N_\eta = 6$. In Section 5.2, we discuss the impact of choosing a different number of membership functions, hence basis functions, to discretize the fault plane.

The initial fault plane discretization is identical for all frequencies and is obtained using the grid partitioning method (Text S1). Figures 2c and 2d show the initial 1D membership functions for ξ (along-strike) and η (updip). Figure 2e shows the initial 2D base function $\overline{W}_{i\xi=3,i\eta=3}$, which in this example results from the combination of the third membership function along-strike with the third membership function in the dip direction. For the case shown in Figure 2c, and considering that each membership function is described by two parameters (μ, σ), we need a total of 24 parameters to describe the basis functions, 12 along-strike and another 12 down-dip. In addition, we require another 36 (6×6) fuzzy amplitude parameters. Thus, the total number of parameters used to describe the spatial slip distribution adds up to 60.

3.3. Inversion

Our inversion finds the solution to the normal Equation 22, presented in Section 2.2.3, for all frequency points. At the current stage of development, this search is performed independently for each frequency. Before starting the inversion, we find the optimal smoothness parameter (α) for each frequency, considering the initial fuzzy membership functions. For this purpose, we compute L-curves for the different frequencies (Figure 3). L-curves show very sharp corners at relatively low frequencies (in this example, at $f \lesssim 11 / 32 \approx 0.3$ Hz), indicating a good ability to resolve the optimal trade-off between smoothness and misfit, that is, to find the smoothest model that can fit the data well. However, the sharpness of the L-curve corners decreases with increasing frequency, indicating that the optimal trade-off between smoothness and data fit cannot be adequately resolved at higher frequencies (in this example, at $f \gtrsim 11 / 32 \approx 0.3$ Hz).

Once α is set, the ANFIS parameters (i.e., the adaptive basis functions and their coefficients) are obtained from the data using the regularized hybrid learning methodology (Section 2.2.3 and Text S2). Note that α is set at the beginning of the learning procedure, before initiating the iterative hybrid optimization, and not updated throughout learning. If we updated α at each learning epoch, we would learn the network with different cost functions at different epochs. This would correspond to solving different minimization problems at different epochs, which would destabilize the inversion. We will discuss the implications of assuming a constant α in Section 5.4.

The inversion stops when the cost function arrives at a stationary point, indicating that the parameters that approximate the slip distribution have converged (Figure 4). Figure 5 compares the 2D fuzzy basis functions for the spatial slip distribution at zero frequency (static slip distribution), $\overline{\mathbf{W}}_0$, at the begging and at the end of learning.
$\overline{}_{32}$
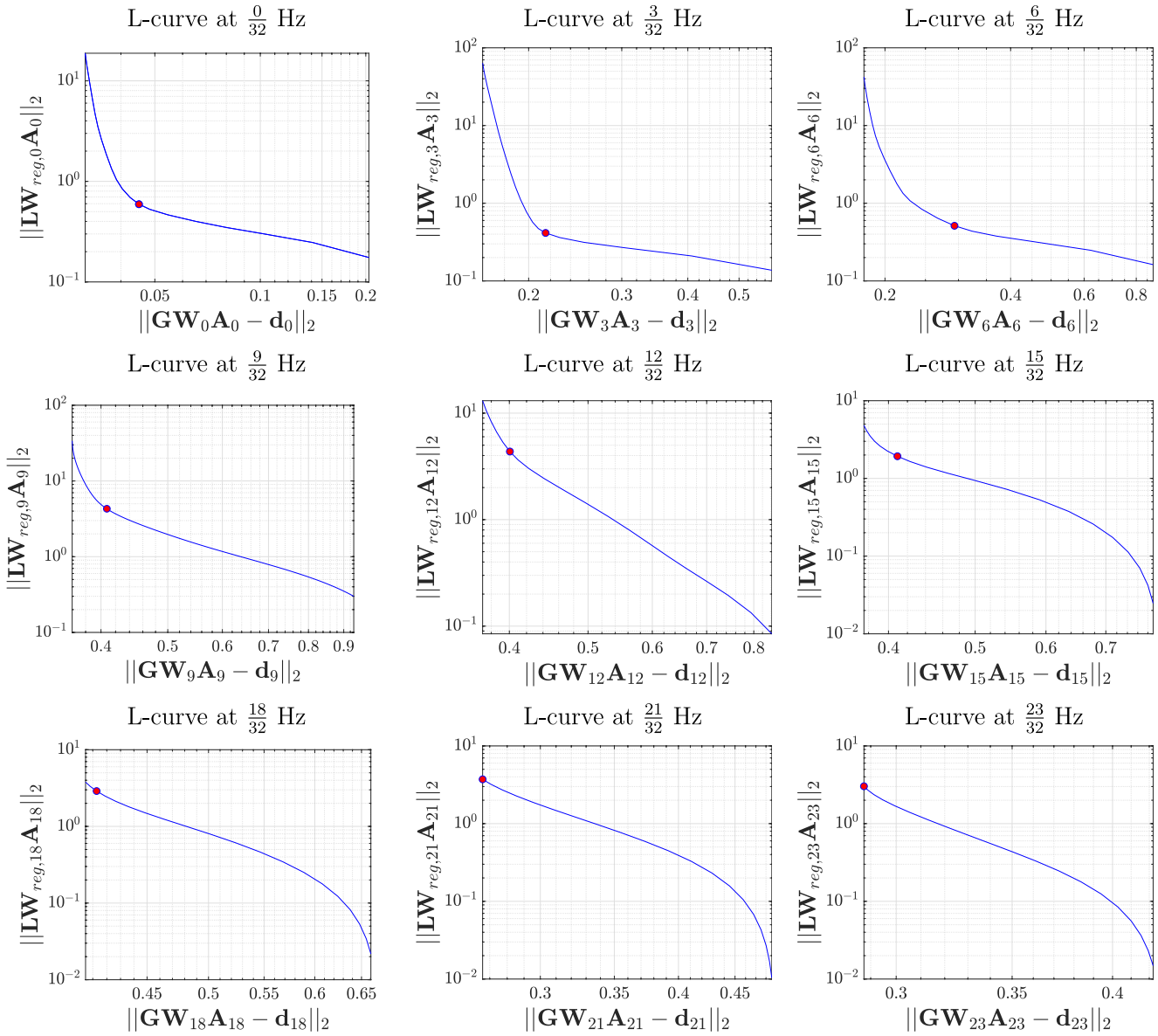
Figure 3. L-curves showing data misfit ($\|\mathbf{GF}_{\omega_j}\mathbf{A}_{\omega_j} - \mathbf{d}_{\omega_j}\|_2$) versus slip roughness ($\|\mathbf{LW}_{\omega_j}\mathbf{A}_{\omega_j}\|_2$) for selected frequency points (ω_j) ranging from 0 to $\frac{23}{32} \approx 0.72Hz$. We used a total of 36 basis functions to describe the spatial slip distribution at every frequency ($N_\xi = 6$, $N_\eta = 6$). The L-curve corners at low frequencies are much clearer than at high frequencies, suggesting that the data can resolve adequately the optimal smoothness level at low frequencies but not at high frequencies. Red circles show the points of maximum curvature. This figure for the full range of solution frequencies is provided in the supplemental material (Figure S7).

4. Results

Figure 6 compares the spatial distributions of slip rate made available by SIV1 and inferred from the neuro-fuzzy method, at selected frequencies. Note that the $f = 0$ Hz model corresponds to the permanent static displacement on the fault, that is, to the final cumulative displacement. A similar comparison for the complete range of frequency points, from 0 to 0.72 Hz, is provided in the supplementary material (Figure S8).

A visual analysis of the true (right) versus inferred (left) slip rate functions shows that the match between the two is good at low frequencies and gradually decreases with increasing frequency. However, at all frequencies, the inversion is able to find the spot on the fault that radiates most energy. These results suggests
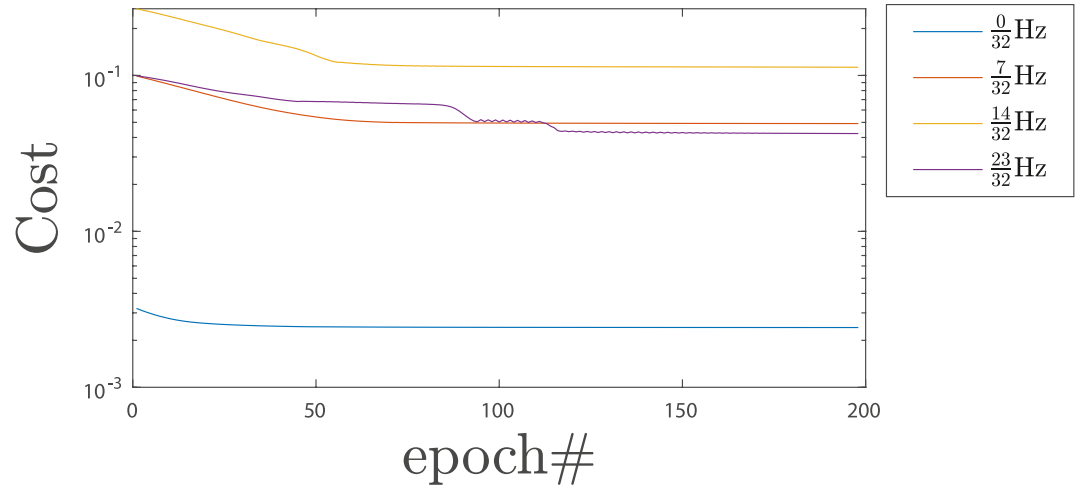
Figure 4. Evolution of the cost function over 200 learning epochs, for selected frequencies $\frac{0}{32} = 0$ Hz, $\frac{7}{32} \approx 0.22$ Hz, $\frac{14}{32} \approx 0.44$ Hz, and $\frac{23}{32} \approx 0.72$ Hz using a total of 36 basis functions ($N_\xi = 6$, $N_\eta = 6$). Note that the convergence to the final solution is faster at low frequencies and slower at high frequencies.

that, while the neuro-fuzzy methodology is adequate at low frequencies, there is still room for improvement at high frequencies. This topic will be further addressed in Section 5.2.

The time-domain slip rate function, $SVF(\xi, \eta, t)$, can be straightforwardly reconstructed from the frequency-domain solutions, $SVF(\xi, \eta, \omega)$, using a simple inverse Fast Fourier transform. We can then inspect the match between the inverted (Figure 7a) and true time-domain slip rate functions (Figure 7b) at chosen points on the fault (Figure 7a). Because the maximum frequency used in our inversion was $\frac{23}{32} \approx 0.72$ Hz, we compare SVFs only below this frequency (Figure 7c, blue line). Figure 7c shows that the fit between inverted (green line) and true SVFs is qualitatively good. Note that the modeled SVFs show negative velocities corresponding to backslip, which are not physically plausible. The backslip is a numerical artifact due to a terminated summation of time-harmonic functions, which is unavoidable in a frequency-domain inversion (e.g., Fan et al., 2014). However, the backslip is limited by the stability of the inversion. Further discussion on backslip in a real earthquake application can be found in the companion article (Kheirdast et al., 2020).
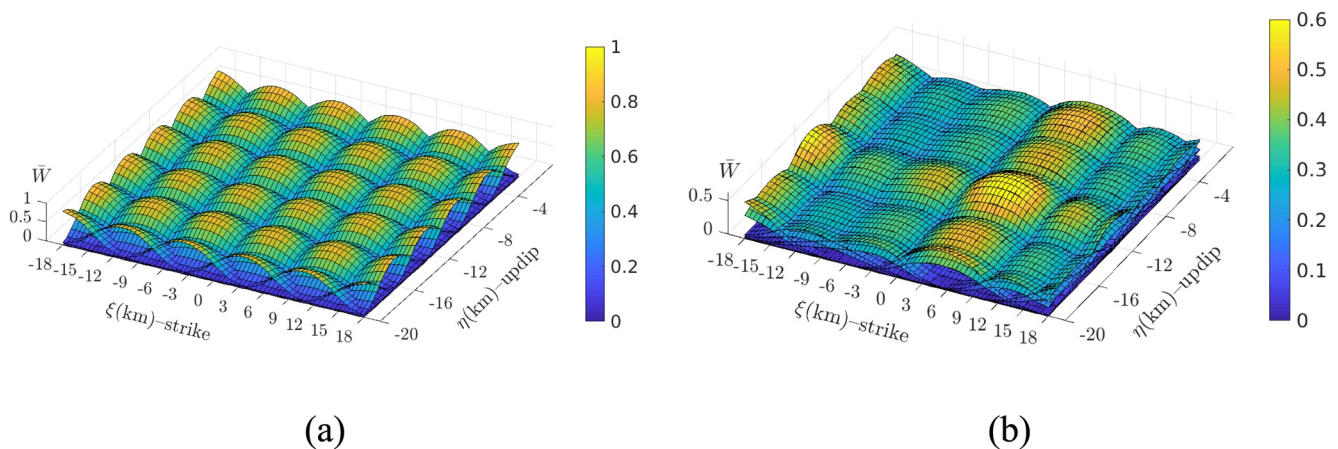
Figure 5. 2D fuzzy basis functions, $\overline{W}_{i_\xi, i_\eta}$, for $f = 0$ Hz. (a) At the beginning of the learning procedure. (b) At the end of the learning procedure.
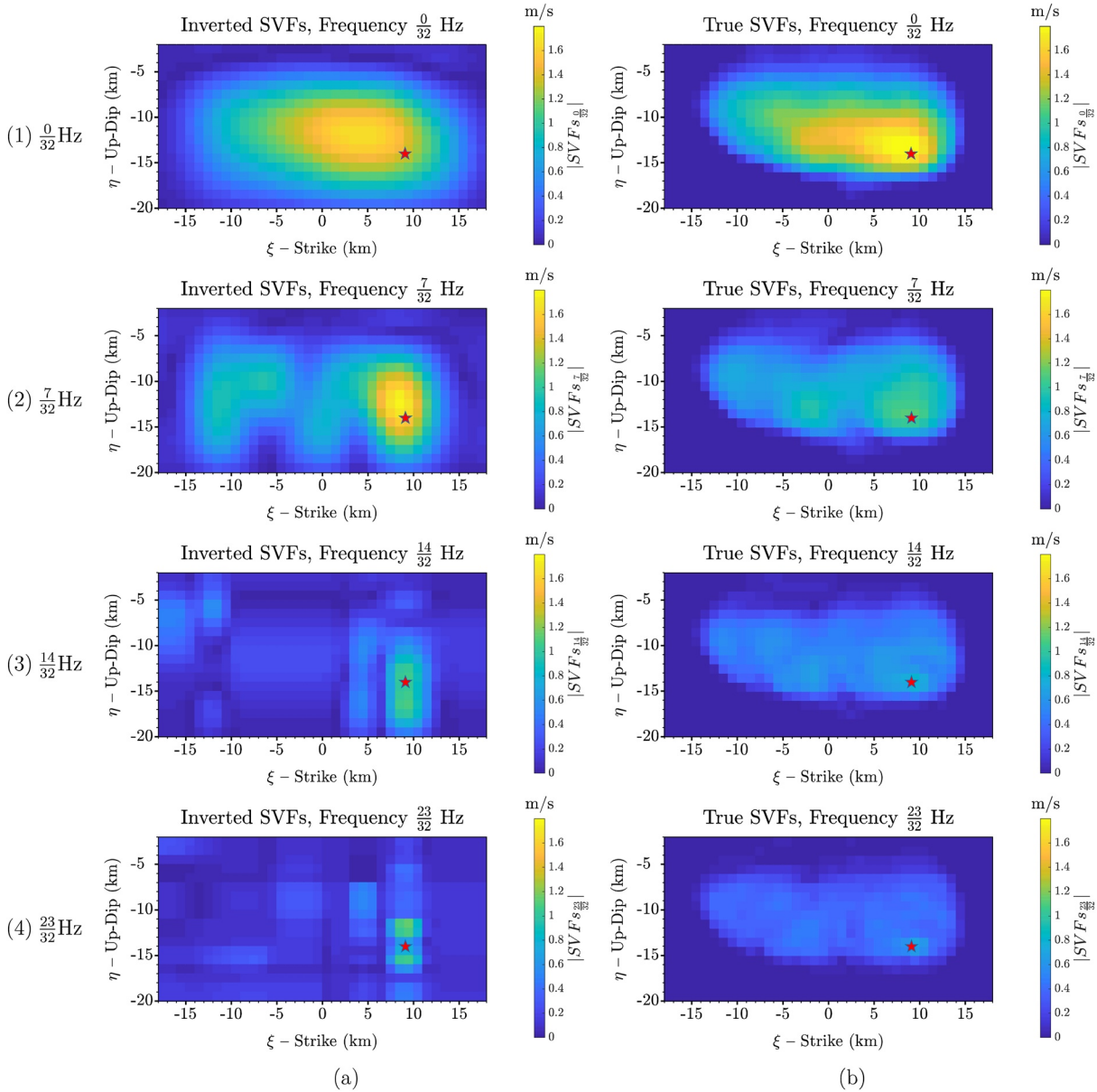
Figure 6. Comparison between the spatial distribution of inverted (a, left) and true (b, right) source velocity functions (SVFs), that is, slip rate, at selected frequency points: (1) $\frac{0}{32} = 0$ Hz, (2) $\frac{7}{32} \approx 0.22$ Hz, (3) $\frac{14}{32} \approx 0.44$ Hz, and (4) $\frac{23}{32} \approx 0.72$ Hz. The slip rate is well retrieved at low frequencies, but becomes less accurate at high frequencies. For all frequencies, we used the same number of membership functions along-strike and updip, $N_\xi = N_\eta = 6$, adding up to a total of 36 basis functions. A similar figure but showing the full range of solution frequencies is provided in the supplemental material (Figure S8).

Figure 8 shows the fit between the original SIV-inv1 waveforms and those generated by our slip model. Again, because the maximum frequency used in our inversion was $\frac{23}{32} \approx 0.72$ Hz, we compare the waveforms only below this frequency. The comparison shows that the main waveform features are very well resolved. However, some of the synthetic waveforms generated by our model have spurious high-frequency ripples.

5. Discussion

Let us now discuss the advantages, limitations and potential improvements of the fuzzy inversion method. The main advantage of the fuzzy inversion method is that it allows to lower the number of spatial basis functions at each frequency, thus strongly reducing the model null-space and stabilizing the inversion.
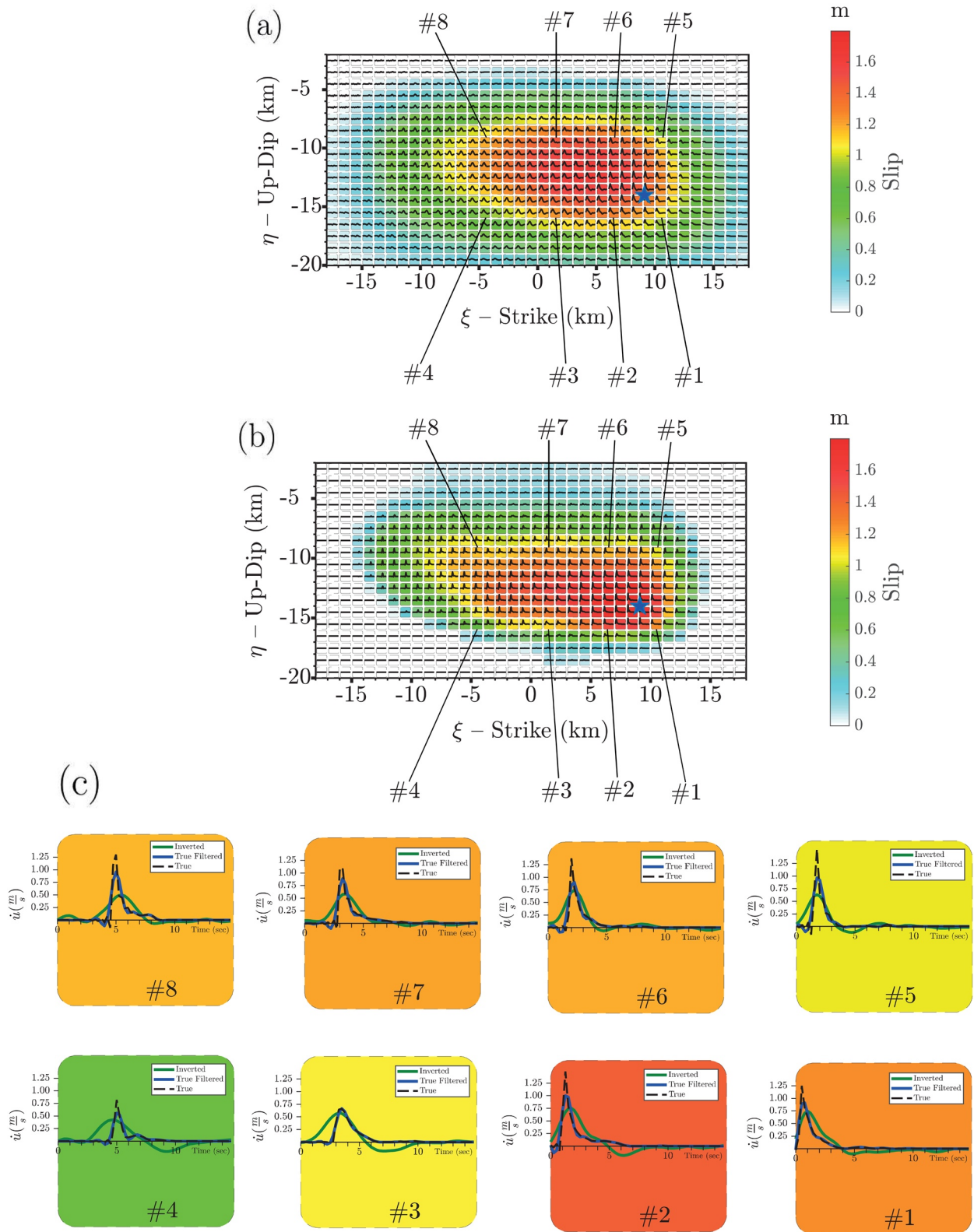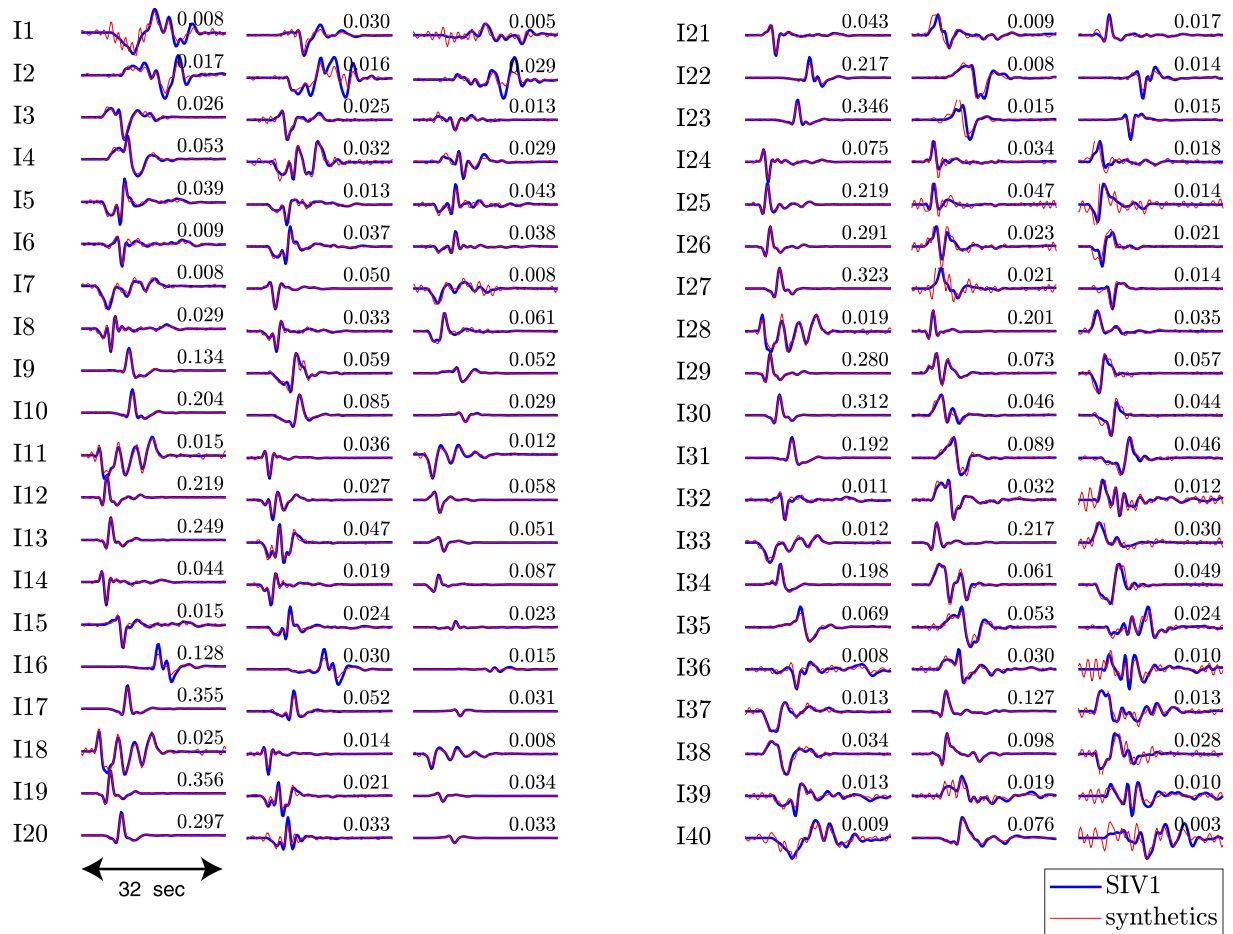
Figure 7.

Figure 8. Comparison between Source Inversion Validation (SIV)-inv1 data (blue) and waveforms generated by our modeled slip distribution (red), at $f < \frac{23}{32} \approx 0.72$ Hz. All main waveform features are well resolved, however some synthetic waveforms generated by our model have spurious high-frequency ripples.

Because the ANFIS approximation uses both linear and nonlinear parameters, a full assessment of model uncertainty will have to evaluate the uncertainty at both the linear and nonlinear steps of the hybrid inversion. Advanced tools in modern statistics and machine learning that allows to reliably determine the quality of solutions include resampling methods (James et al., 2013). These methods involve repeatedly drawing subset to obtain additional information about the model and its uncertainty, such as the variability of the residual norm or model parameters. Two of the most common resampling methods are cross-validation and bootstrap. Cross-validation, and associated variants, like Leave-One-Out Cross-validation (LOOCV) and k-Fold Cross-validation, can be used to estimate the test error associated with a given learning method or to select a specific model among possible choices. In the companion article (Kheirdast et al., 2020), we show a basic cross-validation analysis in a real earthquake application by dividing the data available into two sets: training and validation sets.

Bootstrap is another statistical analysis tool that is widely used to quantify the uncertainty associated with a given estimator or learning method (James et al., 2013). In bootstrap, we randomly select an observation

Figure 7. (a) Location of eight representative cells on the fault plane, for which we compare the true and modeled time-domain slip rate functions. The inverted static slip distribution ($f = 0$ Hz) is plotted in the background. Inverted slip rates are plotted inside each cell. (b) Same as (a) but for the true SIV-1 slip distribution. (c) Enlarged representation of chosen cells in (a, b), showing the comparison of time-domain slip rate functions (SVFs). The background color shows the true static slip (b). The maximum frequency used in our inversion is $\frac{23}{32} \approx 0.72$ Hz, therefore we show the original SIV-inv1 SVF (dashed black line), low-pass filtered at 0.72 Hz (blue line), and the inverted SVF (green), which naturally only contains frequencies <0.72 Hz.

from the data set to produce a bootstrap data set. Several data sets are then used to infer several slip models, from which the uncertainty of the inferred model is determined. Further, in recent advances in fuzzy function approximation methods, Kosko (2018) introduced a generalized mix of additive fuzzy systems and its corresponding mixed probability density. Based on it, one can decide which rule basis system is most adequate for approximating a target data. Using a Monte Carlo sampling, one can find the most adequate system, as well as its uncertainty.

Although a full implementation of these advanced methods of uncertainty estimation is out of the scope of this article, we can still gain insight on the stability of our model by applying generalized singular value decomposition (GSVD) principles (Text S4) at the linear step of our inversion. Therefore, we use GSVD to investigate the effectiveness of the neuro-fuzzy inversion method in mitigating ill posedness throughout the consecutive linear steps of learning epochs. In particular, we investigate how ill posedness depends on the number of membership functions. We also show how the evolutionary nature of the neuro-fuzzy inversion allows to explore both model space and data space while searching for an optimal model.

We discuss how the regularization parameter α evolves throughout optimization and show that assuming a constant α is a valid premise. We discuss the impact of meshing on the numerical stability of the method, as well as the trade-off between resolution and stability. Finally, we evaluate the performance of our method using the multi-dimensional scaling (MDS) introduced by Razafindrakoto et al. (2015).

5.1. Generalized Singular Value Decomposition (GSVD) Applied to the Neuro-Fuzzy Inversion Method

In order to understand how the neuro-fuzzy method mitigates the ill posedness of finite-fault inversions, let us apply generalized singular value decomposition GSVD at the linear step of the hybrid learning scheme, where regularization is applied (Equation 22). The mathematical principles of GSVD are laid out in Text S4. GSVD shows how model space is mapped into data space. Based on GSVD, it is possible to determine coefficients $f_i = \dfrac{\gamma_i^2}{\gamma_i^2 + \alpha^2}$, commonly called filter factors, which control how much the values $\mathbf{U}_{:,i}^T \mathbf{d}_{\omega_j}$ and $\dfrac{\mathbf{U}_{:,i}^T \mathbf{d}_{\omega_j}}{\gamma_i}$ contribute to $Cost_{data}$ and $Cost_{smooth}$, respectively, as a function of the singular values λ_i and μ_i (Hansen, 1992). The columns of matrix $\mathbf{U}$ makes an ortho-normal set of basis vectors and allows us to expand the data-space. Filter factors control how data is mapped into the cost functions as a function of singular values. Small singular values correspond to combinations of model parameters that have little correspondence on data space, therefore, they cannot be found unambiguously by minimization of the cost function. As such, small singular values destabilize the inversion and should be filtered out. The parameter α represents a cut-off in the filter coefficients that separates the singular values that will be used in the inversion from those that will be filtered out. In GSVD, the generalized singular values (γ_i) are arranged in ascending order, therefore f_i represents a high-pass filter (Figures 9a and 9e). In the cost of model roughness (Equation S28), small generalized singular values (γ_i) and consequently small filter coefficients (f_i) correspond to a stop-band, damping large values of $\dfrac{\mathbf{U}_{:,i}^T \mathbf{d}_{\omega_j}}{\gamma_i}$. Inversely, in the cost of data misfit (Equation S30), ($1 - f_i$) represents a low-pass filter (Figures 9b and 9f), which damps large values of $\mathbf{U}_{:,i}^T \mathbf{d}_{\omega_j}$.

Figure 9 shows the values of GSVD factors, namely the filter factors, the coefficients that contribute to $Cost_{data}$, $1 - f_i$, $\mathbf{U}_{:,i}^T \mathbf{d}_{\omega_j}$, and the coefficients that contribute to $Cost_{smooth}$, f_i, $\dfrac{\mathbf{U}_{:,i}^T \mathbf{d}_{\omega_j}}{\gamma_i}$, as a function of the generalized singular values γ_i at two sample frequency points: 0 Hz and $\dfrac{14}{32} \approx 0.44$ Hz. At 0 Hz, the configuration of $\dfrac{\mathbf{U}_{:,i}^T \mathbf{d}_{\omega_j}}{\gamma_i}$ (Figure 9c) and $\mathbf{U}_{:,i}^T \mathbf{d}_{\omega_j}$ (Figure 9d) is such that we can effectively find a cut-off parameter α that separates large values of $\mathbf{U}_{:,i}^T \mathbf{d}_{\omega_j}$, that is, singular values that map well data to the cost function, from large values of $\dfrac{\mathbf{U}_{:,i}^T \mathbf{d}_{\omega_j}}{\gamma_i}$, that is, from destabilizing singular values. Consequently, we can effectively separate
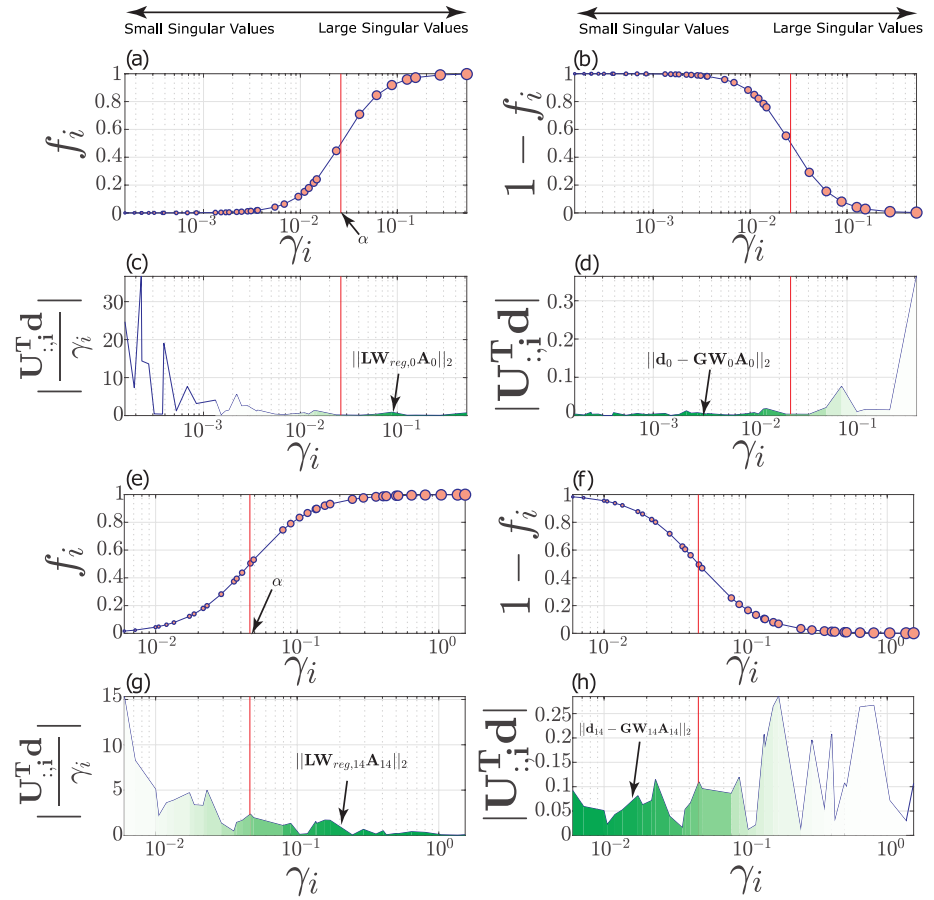
Figure 9. Generalized singular value decomposition of the regularized normal equation solved in the inversion (Equation 22) for (a–d) 0 Hz and (e–h) $\frac{14}{32} \approx 0.44$ Hz. (a, e) Filter factors, $f_i = \frac{\gamma_i^2}{\gamma_i^2 + \alpha^2}$, which correspond to a high-pass filter that controls the contribution of small singular values to the inversion. The cut-off point α (vertical red line) is determined considering the maximum curvature of the L-curve. Circle size corresponds to the value of each generalized singular value. (b, f) $(1 - f_i)$ Low-pass filter that suppresses the effect of large $\mathbf{U}_{:,i}^T\mathbf{d}$ in order to optimize data fit (Equation S30). (c, g) Values of $\frac{\mathbf{U}_{:,i}^T\mathbf{d}}{\gamma_i}$ (see Equation S28) as a function of generalized singular values (γ_i). Note that the large values of $\frac{\mathbf{U}_{:,i}^T\mathbf{d}}{\gamma_i}$ are all placed in the stop-band of f_i, therefore they are effectively filtered out of the inversion. Note that $Cost_{smooth}$ corresponds to the shaded area under this curve. (d, h) Values of $\mathbf{U}_{:,i}^T\mathbf{d}$ as a function of generalized singular values (γ_i). Large values of $\mathbf{U}_{:,i}^T\mathbf{d}$ correspond to the singular values that explain data better. Note that at higher frequencies (in this case, at $f = \frac{14}{32} \approx 0.44$ Hz) the data vector has a larger image on $\mathbf{U}_{:,i}$ corresponding to small singular values (γ_i). $Cost_{data}$ is the squared summation of $\mathbf{U}_{:,i}^T\mathbf{d}$ filtered by $(1 - f_i)$, which corresponds to shaded areas in (d, h). All plots correspond to the slip distribution at the start (epoch 1) of the fuzzy inversion. The number of fuzzy basis functions is $N_\xi = 6$ and $N_\eta = 6$, therefore we have 36 nonzero singular values in this problem setting.

small from large singular values and filter out the destabilizing small singular values. This clear separation between large and small singular values corresponds to an L-curve with a well-defined corner, which indicates a clear optimal trade-off between smoothness and data fit. Note that the smoothness-related cost ($Cost_{smooth}$) corresponds to the shaded area in Figure 9c and the data misfit related cost $Cost_{data}$ corresponds to the shaded area in Figure 9d. In both cases, the darkness of the shaded areas is adjusted by the filter factors, f_i and $1 - f_i$, respectively. On the other hand, at higher frequencies ($\frac{14}{32} \approx 0.44$ Hz in this example), large and small singular values are not as clearly separated. Therefore, it is more difficult to determine an adequate cut-off parameter α at higher frequencies.

5.2. Impact of Varying the Number of Membership Functions.

In Section 4, we showed an example of finding the slip function for the SIV-inv1 benchmark exercise using 6×6 membership functions. In the previous section, we showed that by means of GSVD, we can separate the generalized singular values that help constrain the model parameters from those that make the problem ill posed. The number of model parameters in our inversion scales with the number of membership functions used to discretize the spatial slip distribution. If we use less membership functions, the problem will have a lower number of model parameters. In this case, the parameters will be easier to resolve. However, this imposes model simplicity and the membership functions will not be able to adequately describe the details of a complex slip distribution. On the other hand, if we use more membership functions, it will be more difficult to resolve adequately all model parameters, but they will have a better ability to describe complex slip distributions.

Let us examine what happens when we increase the number of membership functions. In particular, given that high frequencies are the least well resolved in our model, let us consider $f = \frac{14}{32} \approx 0.44$ Hz. Figure 10 compares the GSVD parameters, namely the filter factors ($f_i = \frac{\gamma_i^2}{\gamma_i^2 + \alpha^2}$), $\frac{\mathbf{U}_{:,i}^{\mathbf{T}}d}{\gamma_i}$, and $\mathbf{U}_{:,i}^{T}\mathbf{d}$ at $f = \frac{14}{32} \approx 0.44$ Hz, in inversions where we used a different number of membership functions: $N_\xi = 4, N_\eta = 4$ (Figure 10a), $N_\xi = 5, N_\eta = 5$ (Figure 10b), $N_\xi = 6, N_\eta = 6$ (Figure 10c), $N_\xi = 7, N_\eta = 7$ (Figure 10d), and $N_\xi = 8, N_\eta = 8$ (Figure 10e). This figure shows that the increase in the number of basis functions increases the number of small singular values, therefore, the inversion becomes less well posed and more sensitive to noise perturbations. In general, inversions using less membership functions are less sensitive to noise and reproduce only the main model features.

Because the problem that we are solving is ill posed, the use of regularization strategies is inevitable, thus we always need to select the trade-off parameter α. Note that in the case of the SIV-1 benchmark, where data is noise-free and the true velocity structure and the fault geometry are known, α remains approximately constant for the different examples shown in (Figure 10). In this example, because the estimation of α is reliable and does not depend strongly on number of membership functions, we can increase the number of membership functions as needed to image slip on the fault. However, we should bear in mind that in a real earthquake application increasing the number of membership functions increases the number of small singular values. If finding an adequate α is not possible, then using a lower number of membership functions will prove advantageous.

We should also note that due to the regularization, even if we increase the number of fuzzy basis functions to a very large number, we will still not be able to achieve a perfect solution because of filtering out part of the forward model.

Figure 11 presents the final spatial slip distribution, at $f = \frac{14}{32} \approx 0.44$ Hz, corresponding to the five cases described above, obtained with different numbers of basis functions. The retrieved slip functions are broadly similar to the true slip function. The inversions with the highest number of membership functions ($N_\xi = 8, N_\eta = 8$) is able to resolve more detail. In general, at low frequencies one can adequately resolve the slip function with a lower number of model parameters, whereas at higher frequencies more model parameters are required to explain the data.

5.3. L-Curve Evolution Throughout the Inversion

The learning procedure of the neuro-fuzzy inversion can be seen as an evolutionary method that filters out the parts of the basis functions that do not have a proper image on data and therefore destabilize the inversion. The method keeps the fuzzy basis that allow a proper data fit and improves them throughout consecutive epochs. This procedure continues until a stationary point is reached, where no better data fit can be achieved without generation of instabilities. Next, we discuss the evolutionary power of our learning procedure, which explores both model and data space, by looking at the evolution of L-curves during optimization.
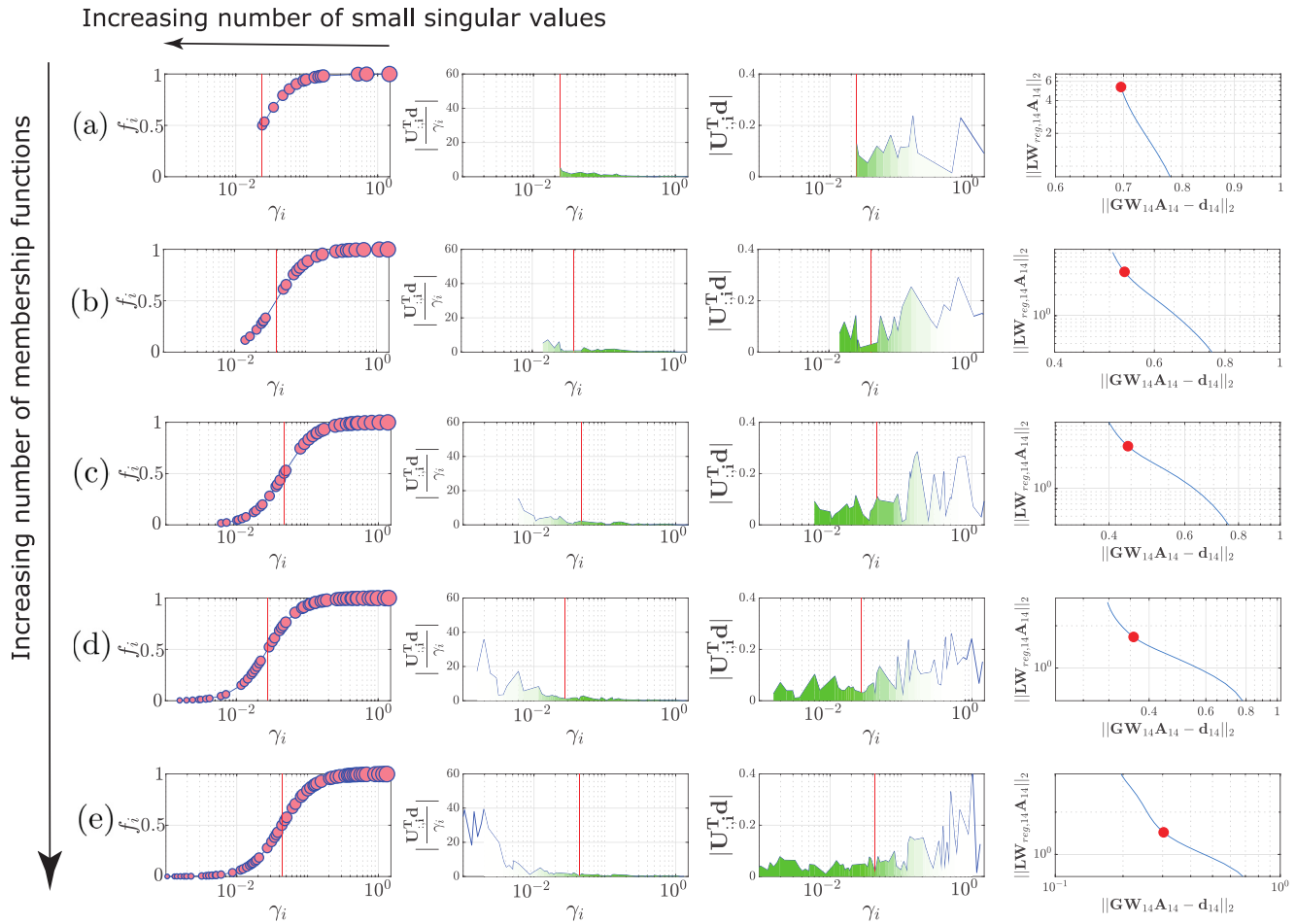
Figure 10. Generalized singular value decomposition (GSVD) analysis for five inversions using different numbers of basis functions. All results concern the slip distribution at $f = \frac{14}{32} \approx 0.44$ Hz, at the first learning epoch, using noise-free data. (a) $N_\xi = 4, N_\eta = 4$, (b) $N_\xi = 5, N_\eta = 5$, (c) $N_\xi = 6, N_\eta = 6$, (d) $N_\xi = 7, N_\eta = 7$, (e) $N_\xi = 8, N_\eta = 8$. The increase in the number of basis functions results in an increase of the number of small singular values. The regularization α parameter (red vertical line) has approximately the same value in all five cases, effectively filtering out small singular values and mitigating their impact. Note that the inversion that uses more basis functions is better able to capture local slip variations (Figure 11).

Figure 12a shows the evolution of the L-curve at 0 Hz through consecutive learning epochs, from 0 to 50. We can see a continuous improvement of the L-curve, such that the optimal smoothness level is reduced at every epoch, while the data misfit does not vary substantially. On the other hand, at higher frequencies ($f = 14 / 32 \approx 0.44$ Hz), both data misfit and slip roughness are reduced throughout learning (Figure 12b).

The results show that the corners of L-curves become sharper throughout the inversion, indicating that as the solution converges the optimal trade-off between data fit and model smoothness becomes better resolved. It also shows that the model evolves differently at different frequencies. Whereas at low frequencies the model improves mostly by decreasing model roughness, at high frequencies data fit improvement is the most relevant feature.

5.4. How Does the Maximum Curvature Point (α) Vary Throughout Learning?

We saw in Section 5.1 that the regularizing parameter α defines the trade-off between data misfit and slip smoothness. In general, the value of α depends on data error and on the predictive power of the forward model. We have already seen that the number of fuzzy basis functions does not impact substantially the value of α (Figure 10). Now, we will investigate the variation of α throughout learning.
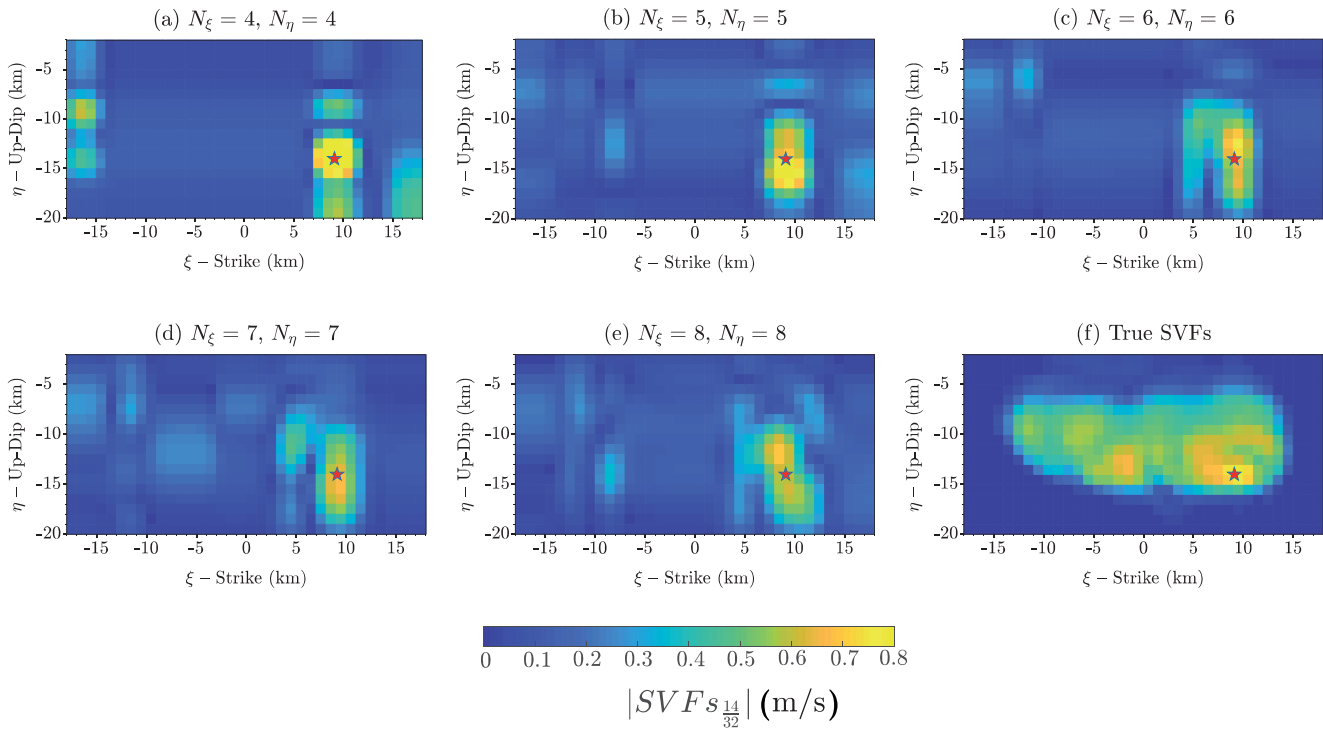
Figure 11. Spatial slip distributions at $f = \frac{14}{32} \approx 0.44$ Hz after 500 learning epochs for the SIV-1 benchmark exercise. Comparison between (a) source velocity function (SVF) retrieved using 16 membership functions: $N_\xi = 4, N_\eta = 4$ (b) SVF retrieved using 25 membership functions: $N_\xi = 5, N_\eta = 5$, (c) SVF retrieved using 36 membership functions: $N_\xi = 6, N_\eta = 6$, (d) SVF retrieved using 49 membership functions: $N_\xi = 7, N_\eta = 7$, (e) SVF retrieved using 64 membership functions: $N_\xi = 8, N_\eta = 8$, and (f) the true SVFs. The inversion that uses more fuzzy basis functions is better able to image the fine-scale structure of the slip distribution.

In our regularization approach, we use α to select the parts of the mathematical model that contribute more to explain our dataset and filter out the remaining parts. This approach is valid if the range of singular values in our problem remains similar throughout learning. If this is not the case, then α must be updated
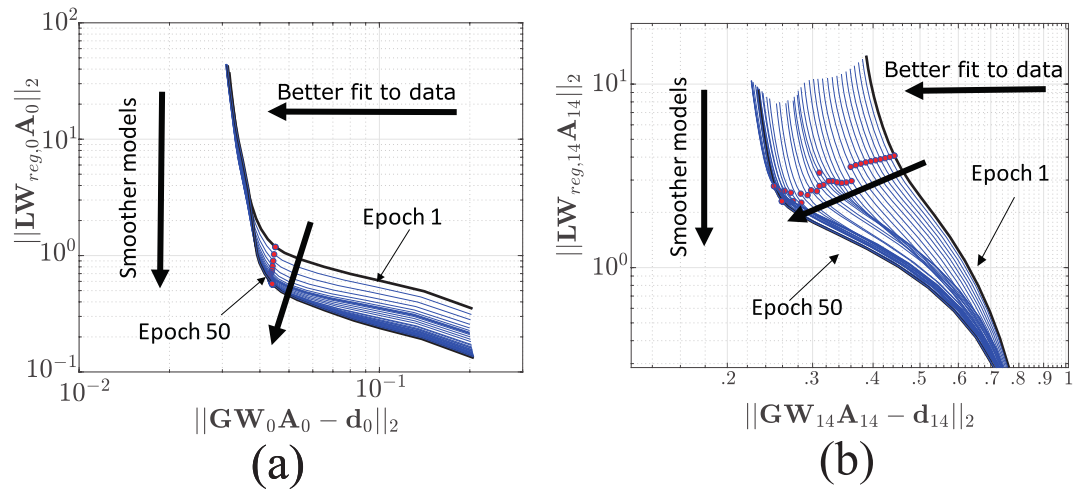
Figure 12. Evolution of L-curves throughout 50 learning epochs at (a) $f = 0$ Hz, and (b) $f = \frac{14}{32} \approx 0.44$ Hz. Over the 50 learning epochs, L-curves move to the bottom and left side of the graphic, indicating that throughout learning we achieve smoother models and better fits to data, respectively.

in order to continue to be effective. As explained in Section 3.3, α is set at the beginning of learning and not updated throughout the optimization. Updating α would correspond to optimizing different cost functions at different iterations, which can destabilize the inversion. However, as the basis functions adaptively evolve, the L-curves also evolve, and so must α. For the sake of this discussion, we display the updated values of α using the L-curve maximum curvature criterion at every single epoch for selected frequencies 0 Hz, $\frac{14}{32} \approx 0.44$ Hz, and $\frac{23}{32} \approx 0.72$ Hz (Figures S9, S10, and S11 in the electronic supplements). The results show that α, as determined from the maximum curvature of the L-curves, in deed varies throughout the inversion but not significantly. Therefore, the constant α approach used in our fuzzy inversion is appropriate.

5.5. Effect of Meshing and Numerical Accuracy in Finding the Damping Parameter α

In Section 5.2, we showed that if we use less membership functions, we can solve the inverse problem with less small singular values, consequently limiting the model null-space and solving a less ill-posed inversion. Ill posedness can be reduced not only by using a low number of membership functions but also by increasing modeling accuracy. In particular, we can reduce ill posedness simply by increasing the number of integration points (N_{gauss}) and decreasing the distance between regularization points (Δx_{reg}). This strategy will increase the forward modeling accuracy and allow a more rigorous regularization. In cases where the trade-off parameter (α) is not detectable from the L-curve, particularly at high-frequencies, this approach can help to determine a proper damping level.

Figure 13 shows four different inversion setups with different numbers of Gaussian integration points and regularizing points. From case#1 to case#4, we continuously increase the number of Gaussian integration points (Figure 13a) and the density of regularizing points (Figure 13b). In all cases, we consider a similar slip discretization, with $N_\xi = 6, N_\eta = 6$ membership functions. The corresponding L-curves, for $f = \frac{9}{32} \approx 0.28$ Hz, are shown in Figure 13c. In case#1, the maximum curvature point is hardly detectable. As the modeling accuracy and constraint power are increased, in case#2, the identification of the trade-off level becomes more clear. In cases #3 and #4, the maximum curvature points have similar residual norms and smoothing level. The L-curve in case#4 is that with a higher curvature, highlighting a better ability to correctly identify the damping parameter (α). The latter cases, #3 and #4, are preferable because they allow for a larger misfit, therefore not overfitting the data as much as cases #1 and #2. By allowing higher misfits and avoiding to overfit the data, less data noise is accounted for, which stabilizes the inversion.

5.6. Resolution

Let us now inspect the resolution of our model. To this end, we compare the model resolution matrix for two cases of slip discretization, at 0 Hz: (1) With constant slip parameters at integration nodes, and (2) With $N_\xi = 6$, $N_\eta = 6$ fuzzy basis functions. In both discretizations, the inversion has 18 integration elements along-strike and 9 updip, adding up to a total of 162 model parameters. We considered one Gaussian point inside each integration element. The regularizing operator $\mathbf{L}$ is similar in the two discretization cases. The configuration of integration and regularization points is as same as case#1 in Figure 13.

First, let us we consider a constant slip discretization. In this case, the model resolution matrix is calculated from (Equation 24):
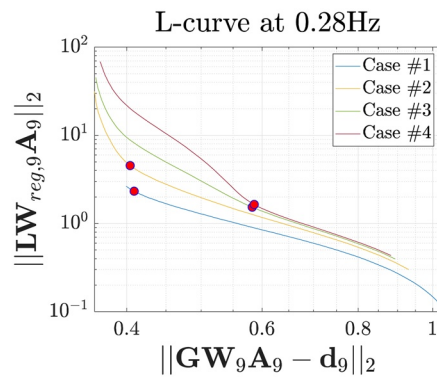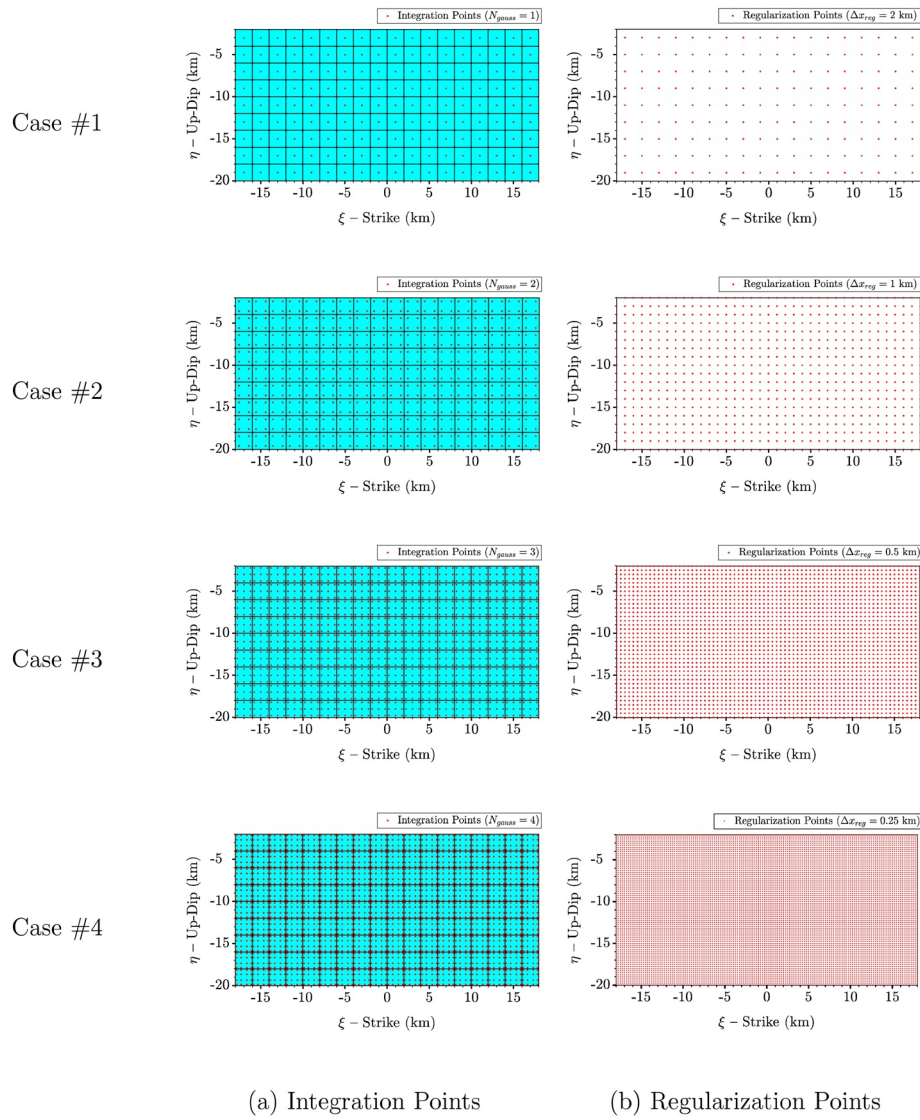
$$\mathbf{Rm}_{\omega_j,\mathbf{C}} = (\mathbf{G}_{\omega_j}^T \mathbf{G}_{\omega_j} + \alpha_C^2 \mathbf{L}^T \mathbf{L})^{-1} \mathbf{G}_{\omega_j}^T \mathbf{G}_{\omega_j}, \tag{24}$$

where $\mathbf{d}_{\omega_j} = \mathbf{G}_{\omega_j} \mathbf{u}_{\omega_j}$ is the forward relationship and $\mathbf{u}_{\omega_j}$ is the slip vector at integration elements.

In the discretization using fuzzy basis functions, we consider the same data as $\mathbf{d}_{\omega_j}$ and try to recover the slip vector $\mathbf{u}_{\omega_j}$ at the final learning epoch. By replacing $\mathbf{A}_{\omega_j}$ from Equation 22 in Equation 19, the model resolution matrix in the fuzzy method $\mathbf{Rm}_{\omega_j,\mathbf{F}}$ becomes:
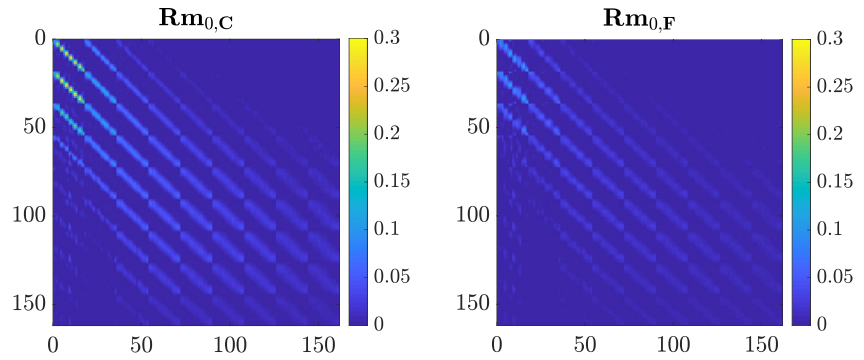
$$\mathbf{Rm}_{\omega_j,\mathbf{F}} = \mathbf{W}_{\omega_j}(\mathbf{GW}_{\omega_j}^T \mathbf{GW}_{\omega_j} + \alpha_F^2 \mathbf{LW}^T \mathbf{LW})^{-1} \mathbf{GW}_{\omega_j}^T \mathbf{G}_{\omega_j} \tag{25}$$

(a) Integration Points

(b) Regularization Points

(c) L-curve

Figure 13.

Figure 14. Resolution matrix at 0 Hz. (a) Resolution of a classical finite fault inversion ($\mathbf{Rm_{0,C}}$), (b) Resolution of the fuzzy inversion after 500 learning epochs ($\mathbf{Rm_{0,F}}$). In the fuzzy inversion, the resolution is decreased in order to increase stability.

In this case, the Gaussian and regularization points are collocated, therefore we omit the subscript, *reg* from $\mathbf{W}_{\omega_j}$.

Figure 14 compares the resolution matrices of cases (1) and (2). The results show that the increased stability of the neuro-fuzzy inversion method reduces the resolution of the model. As expected, model resolution and stability cannot be improved simultaneously. In order to obtain a more reliable model, we must relax model resolution.

5.7. Computational Demand

More fuzzy basis functions will result in a higher resolution of the SVFs, particularly at higher frequencies, provided that Green's functions and data noise do not limit the predictive power of the forward relationship. However, increasing the number of fuzzy basis functions will also increase computation time.

The most time-consuming part of our inversion is the back-propagation (gradient-descent) nonlinear step of hybrid learning. The number of calculations is directly related to the number of connections between consecutive layers of the ANFIS network. The total number of computations for the back-propagation step equals $(N_\xi + N_\eta)(N_\xi N_\eta)$. Thus, the computation time for the gradient descent step alone if ($N_\xi = 6, N_\eta = 6$) is almost 3.4 times more than if ($N_\xi = 4, N_\eta = 4$). Our average CPU time for one epoch of learning for $N_\xi = 6, N_\eta = 6$ is 2.7 s on an Intel(R) Core i5-7400 CPU@3.00 GHz, whereas for $N_\xi = 4, N_\eta = 4$ the average CPU time is 0.82 s (on the same machine). Because in this formulation, we solve independent inverse problems for different frequencies the method can be easily parallelized.

5.8. Multidimensional Scaling

In order to rank the solutions of the SIV benchmark exercises provided by different authors, Razafindrakoto et al. (2015) proposed a multidimensional scaling (MDS) analysis. MDS quantifies the differences between the models obtained by inverse modeling and the true slip function. The aim of MDS analysis is to map dissimilarities between models to Euclidean space, which can be of any dimension but is usually taken as 2D or 3D, such that similar/dissimilar models appear as close/far from each other and can be easily visualized. The dissimilarity between slip functions is quantified using a dissimilarity metrics computed for each pair of slip models. Razafindrakoto et al. (2015) proposed normalized-square and gray-scale metrics for the MDS

Figure 13. Four hypothetical cases used to study the effect of increasing the number of (a) Gaussian integration points and (b) the density of regularizing points. Case #1: Each integration element has one Gaussian point, $N_{gauss} = 1$, and the distance between regularizing points is 2 km, $\Delta x_r = 2$ km. Case #2: $N_{gauss} = 2, \Delta x_r = 1$ km, Case #3: $N_{gauss} = 3, \Delta x_r = 0.5$ km, Case #4: $N_{gauss} = 4, \Delta x_r = 0.25$ km. (c) L-curves, at $f = \frac{9}{32} \approx 0.25$ Hz, for the four cases shown above. In all cases, we used $N_\xi = 6, N_\eta = 6$ fuzzy basis functions. The red circles indicate the maximum curvature points. Increasing the modeling accuracy and the power of the regularizing condition allows for a more appropriate selection of the damping parameter.

analysis. The SIV project (Mai et al., 2016) provides an online toolbox for MDS analysis (http://equake-rc. info/SIV/sivtools/show-scalar-metrics/MDS/inv1/), which allows to compare a given slip model with the true SIV1 slip distribution using the normalized-square metric. Figure S12 shows that the slip model inferred from the fuzzy inversion using 36 fuzzy basis functions ($N_\xi = 6, N_\eta = 6$) is ranked as a good solution. The dissimilarity matrix shows that our method has a dissimilarity index of 7.44 with respect to the original SIV-1, being ranked as the second most similar model to the target after the model of Fan et al. (2014) (fsg, with a dissimilarity index of 3.07).

5.9. Further Developments

The method presented here represents a first step in a new direction that allows for better-posed inversions. The neuro-fuzzy inversion methodology can be applied to any geophysical inverse problem described by a Fredholm integral of the first kind, namely gravity field inversion, fault geometry determination using InSAR data, etc. One important improvement will be to link the slip models at different frequencies, which will further regularize the problem, helping to stabilize the slip patches. As emphasized by Fan et al. (2014), one consequence of formulating the kinematic source problem in the frequency domain is the possible loss of causality in the retrieved solution. Particularly this refers to the obtained phase of the source spectrum. In essential, only time-domain inversion methods, such as Progressive Inversion Strategy (PIS) (Sánchez-Reyes et al., 2018), can explicitly enforce the rupture causality. To prohibit this loss of causality, we probably need to apply a more advanced time-frequency analysis. However, this has not been examined in the current formulation and requires more thorough consideration.

6. Conclusions

We presented a new finite-fault inversion scheme based on machine learning techniques. The inversion is carried out in the frequency domain. At each frequency, the spatial slip distribution is described as a function of a few fuzzy adaptive basis functions, which evolve to allow the most proper fit to data. Thus, the spatial discretization uses only a small number of model parameters. The adequate adaptive basis functions and their amplitudes are found using an Adaptive Network-based Fuzzy Inference System (ANFIS). The learning of the ANFIS is regularized as to optimize the smoothness of the spatial slip distributions. The parameterization of the spatial slip distributions allows to decrease substantially the number of parameters, which strongly decreases the ill posedness of the inverse problem. Using ANFIS for model approximation, we can separate the forward integration mesh from the regularization mesh, thus providing numerical stability to the method. By means of GSVD analysis, we discuss the conditions under which the inversion is well or ill posed. Adequate damping coefficients α are selected from L-curves that display sharp corners. This allows to select a proper set of generalized singular values that render the problem well posed. The proposed method evolves continuously toward smoother models that generate better data fits. In the work presented in this study, we worked with a noise-free dataset. In the companion work (Kheirdast et al., 2020), we show an application with real data. Due to the trade-off between well posedness and resolution, the proposed method has a lower resolution than conventional finite-fault models, which rely on large numbers of model parameters. The MDS analysis shows that our method provides a reliable model, with a good similarity to the true slip function.

Appendix A: List of abbreviations

ANFIS	Adaptive neuro fuzzy inference system
CPU	Central processing unit
FIS	Fuzzy inference system
GA	Genetic algorithms
GF	Green's Function
GMF	Gaussian membership function
GNSS	Global navigation satellite system
GPS	Global positioning system
GSVD	Generalized singular value decomposition

InSAR	Interferometric synthetic-aperture radar
LOOCV	Leave one out cross validation
MCMC	Markov Chain Monte Carlo
MDS	Multidimensional scaling
MF	Membership Function
PSO	Particle swarm optimization
SIV	Source inversion validation
SVF	Source velocity (slip-rate) function

Data Availability Statement

Data used in this study can be accessed from the SIV project (Mai et al., 2016) website from the download page through (http://equake-rc.info/sivdb/wiki/Downloads).

References

Aki, K., & Richards, P. G. (2002). *Quantitative seismology* (2nd ed.). Sausalito, CA: University Science Books.

Archuleta, R. J., & Ji, C. (2016). Moment rate scaling for earthquakes 3.3 m 5.3 with implications for stress drop. *Geophysical Research Letters*, *43*(23), 12004–12011. https://doi.org/10.1002/2016gl071433

Aster, R. C., Borchers, B., & Thurber, C. H. (2018). *Parameter estimation and inverse problems*. Elsevier.

Atkinson, G. M., & Boore, D. M. (2006). Earthquake ground-motion prediction equations for eastern North America. *Bulletin of the Seismological Society of America*, *96*(6), 2181–2205. https://doi.org/10.1785/012005024510.1785/0120050245

Barnhart, W. D., & Lohman, R. B. (2010). Automated fault model discretization for inversions for coseismic slip distributions. *Journal of Geophysical Research*, *115*(B10). https://doi.org/10.1029/2010jb007545

Beresnev, I. A. (2003). Uncertainties in finite-fault slip inversions: To what extent to believe? (a critical review). *Bulletin of the Seismological Society of America*, *12*(6), 2445–2458. https://doi.org/10.1785/012002022510.1785/0120020225

Beresnev, I. A., & Atkinson, G. M. (1997). Modeling finite-fault radiation from the spectrum. *Bulletin of the Seismological Society of America*, *87*(1), 67–84.

Bodin, T., & Sambridge, M. (2009). Seismic tomography with the reversible jump algorithm. *Geophysical Journal International*, *178*(3), 1411–1436. https://doi.org/10.1111/j.1365-246x.2009.04226.x

Bouchon, M. (1997). The state of stress on some faults of the san andreas system as inferred from near-field strong motion data. *Journal of Geophysical Research*, *102*(B6), 11731–11744. https://doi.org/10.1029/97jb00623

Buckley, J. (1992). Universal fuzzy controllers. *Automatica*, *28*(6), 1245–1248. https://doi.org/10.1016/0005-1098(92)90068-q

Causse, M., Dalguer, L. A., & Mai, P. M. (2013). Variability of dynamic source parameters inferred from kinematic models of past earthquakes. *Geophysical Journal International*, *196*(3), 1754–1769. https://doi.org/10.1093/gji/ggt47810.1093/gji/ggt478

Cohen, A. (2003). *Numerical analysis of wavelet methods* (p. 354). Elsevier.

Cotton, F., & Campillo, M. (1995). Frequency domain inversion of strong motions: Application to the 1992 landers earthquake. *Journal of Geophysical Research*, *100*(B3), 3961–3975. https://doi.org/10.1029/94jb02121

Coutant, O. (1989). *Program of numerical simulation AXITRA. Res. Rep. LGIT*. Grenoble: Universite Joseph Fourier (in French).

Coutant, O. (2020). *coutanto/axitra: axitra v2019*. Zenodo. https://doi.org/10.5281/zenodo.3985053

Custódio, S., & Archuleta, R. J. (2007). Parkfield earthquakes: Characteristic or complementary? *Journal of Geophysical Research*, *112*(B5). https://doi.org/10.1029/2006jb004617

Custódio, S., Liu, P., & Archuleta, R. J. (2005). The 2004 Mw6.0 Parkfield, California, earthquake: Inversion of near-source ground motion using multiple data sets. *Geophysical Research Letters*, *32*(23). https://doi.org/10.1029/2005gl024417

Custódio, S., Page, M. T., & Archuleta, R. J. (2009). Constraining earthquake source inversions with GPS data: 2. A two-step approach to combine seismic and geodetic data sets. *Journal of Geophysical Research*, *114*(B1). https://doi.org/10.1029/2008jb005746

Das, S., & Kostrov, B. V. (1990). Inversion for seismic slip rate history and distribution with stabilizing constraints: Application to the 1986 Andreanof Islands earthquake. *Journal of Geophysical Research*, *95*(B5), 6899–6913. https://doi.org/10.1029/JB095iB05p06899

Di Carli, S., François-Holden, C., Peyrat, S., & Madariaga, R. (2010). Dynamic inversion of the 2000 Tottori earthquake based on elliptical subfault approximations. *Journal of Geophysical Research*, *115*(B12). https://doi.org/10.1029/2009jb006358

Engl, H. W., Hanke, M., & Neubauer, A. (1996). *Regularization of inverse problems* (p. 322). Springer Science & Business Media.

Fan, W., Shearer, P. M., & Gerstoft, P. (2014). Kinematic earthquake rupture inversion in the frequency domain. *Geophysical Journal International*, *199*(2), 1138–1160. https://doi.org/10.1093/gji/ggu31910.1093/gji/ggu319

Freed, A. M., & Lin, J. (2001). Delayed triggering of the 1999 hector mine earthquake by viscoelastic stress transfer. *Nature*, *411*(6834), 180–183. https://doi.org/10.1038/3507554810.1038/35075548

Gabriel, A.-A., Ampuero, J.-P., Dalguer, L. A., & Mai, P. M. (2012). The transition of dynamic rupture styles in elastic media under velocity-weakening friction. *Journal of Geophysical Research*, *117*(B9). https://doi.org/10.1029/2012jb009468

Gallovič, F., & Ampuero, J.-P. (2015). A new strategy to compare inverted rupture models exploiting the eigenstructure of the inverse problem. *Seismological Research Letters*, *86*(6), 1679–1689. https://doi.org/10.1785/022015009610.1785/0220150096

Gallovič, F., Imperatori, W., & Mai, P. M. (2015). Effects of three-dimensional crustal structure and smoothing constraint on earthquake slip inversions: Case study of the M$_w$6.3 2009 L'Aquila earthquake. *Journal of Geophysical Research: Solid Earth*, *120*(1), 428–449. https://doi.org/10.1002/2014JB011650

Gallovič, F., & Zahradník, J. (2011). Toward understanding slip inversion uncertainty and artifacts: 2. Singular value analysis. *Journal of Geophysical Research*, *116*(B2). https://doi.org/10.1029/2010JB007814

Green, P. J. (1995). Reversible jump Markov chain Monte Carlo computation and Bayesian model determination. *Biometrika*, *82*(4), 711–732. https://doi.org/10.1093/biomet/82.4.711

Hallo, M., & Gallovič, F. (2020). Bayesian self-adapting fault slip inversion with green's functions uncertainty and application on the 2016 M$_w$7.1 Kumamoto earthquake. *Journal of Geophysical Research: Solid Earth*, *125*(3), e2019JB018703. https://doi.org/10.1029/2019JB018703

Hansen, P. C. (1992). Analysis of discrete ill-posed problems by means of the L-curve. *SIAM Review*, *34*(4), 561–580. https://doi.org/10.1137/103411510.1137/1034115

Hansen, P. C. (2005). *Rank-deficient and discrete ill-posed problems: Numerical aspects of linear inversion* (p. 247). Siam.

Hartzell, S. H., & Heaton, T. H. (1983). Inversion of strong ground motion and teleseismic waveform data for the fault rupture history of the 1979 Imperial Valley, California, earthquake. *Bulletin of the Seismological Society of America*, *12*(6A), 1553–1583. https://doi.org/10.1785/bssa07306a1553

Heaton, T. H. (1990). Evidence for and implications of self-healing pulses of slip in earthquake rupture. *Physics of the Earth and Planetary Interiors*, *64*(1), 1–20. https://doi.org/10.1016/0031-9201(90)90002-f

Hernandez, B., Cocco, M., Cotton, F., Stramondo, S., Scotti, O., Courboulex, F., & Campillo, M. (2004). Rupture history of the 1997 Umbria-Marche (central Italy) main shocks from the inversion of GPS, DInSAR and near field strong motion data. *Annals of Geophysics*, *47*(4). https://doi.org/10.4401/ag-3349

Hutchings, L., Ioannidou, E., Foxall, W., Voulgaris, N., Savy, J., & Kalogeras, I. (2007). A physically based strong ground-motion prediction methodology; application to PSHA and the 1999 M$_w$ = 6.0 Athens earthquake. *Geophysical Journal International*, *168*(2), 659–680. https://doi.org/10.1111/j.1365-246X.2006.03178.x

Hutchings, L., Mert, A., Fahjan, Y., Novikova, T., Golara, A., Miah, M., & Foxall, W. (2018). Physics-based hazard assessment for critical structures near large earthquake sources. *Best practices in physics-based fault rupture models for seismic hazard assessment of nuclear installations* (pp. 311–338). Springer. https://doi.org/10.1007/978-3-319-72709-7_18

James, G., Witten, D., Hastie, T., & Tibshirani, R. (2013). *An introduction to statistical learning* (p. 430). Springer.

Jang, J.-S. R. (1991). Fuzzy modeling using generalized neural networks and Kalman filter algorithm. *AAAI* (pp. 762–767).

Jang, J.-S. R. (1993). ANFIS: Adaptive-network-based fuzzy inference system. *IEEE Transactions on Systems, Man, and Cybernetics*, *23*(3), 665–685. https://doi.org/10.1109/21.256541

Jara, J., Sánchez-Reyes, H., Socquet, A., Cotton, F., Virieux, J., Maksymowicz, A., & Norabuena, E. (2018). Kinematic study of Iquique 2014 M$_w$ 8.1 earthquake: Understanding the segmentation of the seismogenic zone. *Earth and Planetary Science Letters*, *503*, 131–143. https://doi.org/10.1016/j.epsl.2018.09.025

Ji, C., Wald, D. J., & Helmberger, D. V. (2002a). Source description of the 1999 Hector Mine, California, Earthquake, Part II: Complexity of slip history. *Bulletin of the Seismological Society of America*, *92*(4), 1208–1226. https://doi.org/10.1785/012000091710.1785/0120000917

Ji, C., Wald, D. J., & Helmberger, D. V. (2002b). Source description of the 1999 Hector Mine, California, Earthquake, Part I: Wavelet domain inversion theory and resolution analysis. *Bulletin of the Seismological Society of America*, *92*(4), 1192–1207. https://doi.org/10.1785/012000091610.1785/0120000916

Kheirdast, N., Ansari, A., & Custódio, S. (2020). Fuzzy kinematic finite-fault inversion: 2. Application to the M$_w$6.0, 24/August/2016, Amatrice earthquake. *Journal of Geophysical Research: Solid Earth* (submitted)

King, G. C. P., Stein, R. S., & Lin, J. (1994). Static stress changes and the triggering of earthquakes. *Bulletin of the Seismological Society of America*, *84*(3), 935–953.

Kosko, B. (1994). Fuzzy systems as universal approximators. *IEEE Transactions on Computers*, *43*(11), 1329–1333. https://doi.org/10.1109/12.324566

Kosko, B. (2018). Additive fuzzy systems: From generalized mixtures to rule continua. *International Journal of Intelligent Systems*, *33*(8), 1573–1623. https://doi.org/10.1002/int.21925

Liu, P., & Archuleta, R. J. (2004). A new nonlinear finite fault inversion with three-dimensional green's functions: Application to the 1989 Loma Prieta, California, earthquake. *Journal of Geophysical Research*, *109*(B2). https://doi.org/10.1029/2003jb002625

Lohman, R. B., & Simons, M. (2005). Some thoughts on the use of InSAR data to constrain models of surface deformation: Noise structure and data downsampling. *Geochemistry, Geophysics, Geosystems*, *6*(1). https://doi.org/10.1029/2004gc000841

Mai, P. M. (2009). Ground motion: Complexity and scaling in the near field of earthquake ruptures. In R. A. Meyers (Ed.), *Encyclopedia of complexity and systems science* (pp. 4435–4474). New York, NY: Springer. https://doi.org/10.1007/978-0-387-30440-3_263

Mai, P. M., & Beroza, G. C. (2000). Source scaling properties from finite-fault-rupture models. *Bulletin of the Seismological Society of America*, *90*(3), 604–615. https://doi.org/10.1785/011999012610.1785/0119990126

Mai, P. M., Imperatori, W., & Olsen, K. B. (2010). Hybrid broadband ground-motion simulations: combining long-period deterministic synthetics with high-frequency multiple s-to-s backscattering. *Bulletin of the Seismological Society of America*, *100*(5A), 2124–2142. https://doi.org/10.1785/012008019410.1785/0120080194

Mai, P. M., Schorlemmer, D., Page, M., Ampuero, J., Asano, K., Causse, M., & Zielke, O. (2016). The earthquake-source inversion validation (SIV) project. *Seismological Research Letters*, *87*(3), 690–708. https://doi.org/10.1785/022015023110.1785/0220150231

Mai, P. M., & Thingbaijam, K. K. S. (2014). SRCMOD: An online database of finite-fault rupture models. *Seismological Research Letters*, *85*(6), 1348–1357. https://doi.org/10.1785/022014007710.1785/0220140077

Massonnet, D., & Feigl, K. L. (1998). Radar interferometry and its application to changes in the earth's surface. *Reviews of Geophysics*, *36*(4), 441–500. https://doi.org/10.1029/97rg03139

Minson, S. E., Simons, M., & Beck, J. L. (2013). Bayesian inversion for finite fault earthquake source models I: Theory and algorithm. *Geophysical Journal International*, *194*(3), 1701–1726. https://doi.org/10.1093/gji/ggt18010.1093/gji/ggt180

Minson, S. E., Simons, M., Beck, J. L., Ortega, F., Jiang, J., Owen, S. E., & Sladen, A. (2014). Bayesian inversion for finite fault earthquake source models – II: The 2011 great Tohoku-oki, Japan earthquake. *Geophysical Journal International*, *198*(2), 922–940. https://doi.org/10.1093/gji/ggu17010.1093/gji/ggu170

Nissen, E., Ghods, A., Karasözen, E., Elliott, J. R., Barnhart, W. D., Bergman, E. A., & Chen, L. (2019). The 12 November 2017 M$_w$ 7.3 Ezgeleh-Sarpolzahab (Iran) earthquake and active tectonics of the Lurestan arc. *Journal of Geophysical Research: Solid Earth*, *124*(2), 2124–2152. https://doi.org/10.1029/2018jb016221

Olson, A. H., & Anderson, J. G. (1988). Implications of frequency-domain inversion of earthquake ground motions for resolving the space-time dependence of slip on an extended fault. *Geophysical Journal International*, *94*(3), 443–455. https://doi.org/10.1111/j.1365-246X.1988.tb02267.x

Olson, A. H., & Apsel, R. J. (1982). Finite faults and inverse theory with applications to the 1979 Imperial Valley earthquake. *Bulletin of the Seismological Society of America*, *12*(6A), 1969–2001. https://doi.org/10.1785/bssa07206a1969

Page, M. T., Dunham, E. M., & Carlson, J. M. (2005). Distinguishing barriers and asperities in near-source ground motion. *Journal of Geophysical Research*, *110*(B11). https://doi.org/10.1029/2005jb003736

Razafindrakoto, H. N. T., Mai, P. M., Genton, M. G., Zhang, L., & Thingbaijam, K. K. S. (2015). Quantifying variability in earthquake rupture models using multidimensional scaling: Application to the 2011 Tohoku earthquake. *Geophysical Journal International*, *202*(1), 17–40. https://doi.org/10.1093/gji/ggv08810.1093/gji/ggv088

Rezakazemi, M., Dashti, A., Asghari, M., & Shirazian, S. (2017). H2-selective mixed matrix membranes modeling using ANFIS, PSO-AN-FIS, GA-ANFIS. *International Journal of Hydrogen Energy*, *42*(22), 15211–15225. https://doi.org/10.1016/j.ijhydene.2017.04.044

Ripperger, J., & Mai, P. M. (2004). Fast computation of static stress changes on 2D faults from final slip distributions. *Geophysical Research Letters*, *31*(18). https://doi.org/10.1029/2004gl020594

Sánchez-Reyes, H. S., Tago, J., Métivier, L., Cruz-Atienza, V. M., & Virieux, J. (2018). An evolutive linear kinematic source inversion. *Journal of Geophysical Research: Solid Earth*, *123*(6), 4859–4885. https://doi.org/10.1029/2017jb015388

Satake, K., Fujii, Y., Harada, T., & Namegaya, Y. (2013). Time and space distribution of coseismic slip of the 2011 Tohoku earthquake as inferred from tsunami waveform data. *Bulletin of the Seismological Society of America*, *103*(2B), 1473–1492. https://doi.org/10.1785/012012012210.1785/0120120122

Sen, M. K., & Biswas, R. (2017). Transdimensional seismic inversion using the reversible jump Hamiltonian Monte Carlo algorithm. *Geophysics*, *82*(3), R119–R134. https://doi.org/10.1190/geo2016-0010.1

Stein, R. S., Barka, A. A., & Dieterich, J. H. (1997). Progressive failure on the North Anatolian fault since 1939 by earthquake stress triggering. *Geophysical Journal International*, *128*(3), 594–604. https://doi.org/10.1111/j.1365-246X.1997.tb05321.x

Takagi, T., & Sugeno, M. (1983). Derivation of fuzzy control rules from human operator's control actions. *IFAC proceedings volumes* (pp. 55–60). Marseille. Retrieved from IFAC Symposium on Fuzzy Information, Knowledge Representation and Decision Analysis. https://doi.org/10.1016/S1474-6670(17)62005-6

Thingbaijam, K. K. S., Martin Mai, P., & Goda, K. (2017). New empirical earthquake source-scaling laws. *Bulletin of the Seismological Society of America*, *107*(5), 2225–2246. https://doi.org/10.1785/0120170017

Tinti, E., Fukuyama, E., Piatanesi, A., & Cocco, M. (2005). A kinematic source-time function compatible with earthquake dynamics. *Bulletin of the Seismological Society of America*, *95*(4), 1211–1223. https://doi.org/10.1785/012004017710.1785/0120040177

Twardzik, C., Madariaga, R., Das, S., & Custódio, S. (2012). Robust features of the source process for the 2004 Parkfield, California, earthquake from strong-motion seismograms. *Geophysical Journal International*, *191*(3), 1245–1254. https://doi.org/10.1111/j.1365-246X.2012.05653.x

Vallée, M., & Bouchon, M. (2004). Imaging coseismic rupture in far field by slip patches. *Geophysical Journal International*, *156*(3), 615–630. https://doi.org/10.1111/j.1365-246X.2004.02158.x

Wang, L.-X. (1992). Fuzzy systems are universal approximators. *[1992 proceedings] IEEE international conference on fuzzy systems* (pp. 1163–1170). https://doi.org/10.1109/FUZZY.1992.258721

Wang, L.-X., & Mendel, J. M. (1992). Fuzzy basis functions, universal approximation, and orthogonal least-squares learning. *IEEE Transactions on Neural Networks*, *3*(5), 807–814. https://doi.org/10.1109/72.159070

Zafarani, H., Noorzad, A., Ansari, A., & Bargi, K. (2009). Stochastic modeling of Iranian earthquakes and estimation of ground motion for future earthquakes in greater Tehran. *Soil Dynamics and Earthquake Engineering*, *29*(4), 722–741. https://doi.org/10.1016/j.soildyn.2008.08.002